



ISSN 2521-6368

Volume 8
Number 2
2024

Journal of Baku Engineering University

P H Y S I C S

Journal is published twice a year
Number-1. June, Number-2. December

An International Journal

<http://journal.beu.edu.az>

Editor-in-chief

Niftali Qocayev

Co-Editor

Razim Bayramli

Editorial advisory board

- Ahmed Abidinov (Baku State University, Azerbaijan)*
Aleksey Shaytan (Moscow State University, Russia)
Ali Javan (Massachusetts Institute of Technology, USA)
Alim Hasanov (Baku State University, Azerbaijan)
Anar Rustamov (Hote Frankfurt University, Germany)
Andrey Rubin (Moscow State University, Russia)
Aysen E. Ozel (Istanbul University, Turkey)
Eden Mahmut (Black Sea Universities Network Center, Romania)
Eldar Masimov (Baku State University, Azerbaijan)
Farhad Rustamov (Institute of Physical Problems, Azerbaijan)
Garib Murshudov (York Academy, UK, London)
Gulnara Akhverdievova (Institute of Physical Problems, Azerbaijan)
Gulshen Agayeva (Institute of Physical Problems, Azerbaijan)
Hatam Mahmudlu (Institute of Photonics, Leibniz University Hannover, Hannover, Germany)
Ilmutdin Abdulaqatov (National Institute of Standards and Technology, Russia)
Irada Aliyeva (Baku State University, Azerbaijan)
Izzat Afandiyeva (Baku State University, Azerbaijan)
Jahangir Guseynov (Azerbaijan Pedagogical University, Azerbaijan)
Kamran Mahmudov (University of Lisbon, Portugal)
- Konstantin Shaitan (Moscow State University, Russia)*
Larisa Ismayilova (Institute of Physical Problems, Azerbaijan)
Nadir Gahramanov (Baku State University, Azerbaijan)
Namiq Ahmedov (Institute of Physical Problems, Azerbaijan)
Natiq Atakishiyev (Universidad Nacional Autonoma de Mexico)
Rasim Mamedov (Baku State University, Azerbaijan)
Rauf Jafarov (Institute of Physical Problems, Azerbaijan)
Sajida Abdulvahabova (Baku State University, Azerbaijan)
Sevim Akyuz (Science and Letter Faculty, Istanbul Kultur University, Turkey)
Sefa Celik (Istanbul University, Turkey)
Suleyman Allakhverdiev (Russian Academy Science, Moscow)
Svetlana Demuhamedova (Institute of Physical Problems, Azerbaijan)
Takhmasib Aliyev (METU, Ankara, Turkey)
Taleh Yusifov (University of California, USA, Los Angeles)
Tarana Aliyeva (Institute of Physical Problems, Azerbaijan)
Taryel Ismayilov (Institute of Physical Problems, Azerbaijan)
Vagif Nasirov (Azerbaijan Pedagogical University, Azerbaijan)
Veli Gusseyinov (National Academy of Science, Azerbaijan)
Mubariz Mammadov (Baku State University, Azerbaijan)

Executive Editors

Shafag Alizade

Assistant Editors

Ulker Agayeva

Lala Hajiyeva

Design

Ilham Aliyev

Contact address

Journal of Baku Engineering University
AZ0102, Khirdalan city, Hasan Aliyev str. 120, Absheron, Baku, Azerbaijan

Tel: 00 994 12 - 349 99 95 **Fax:** 00 994 12 349-99-90/91

e-mail: jr-physics@beu.edu.az

web: <http://journal.beu.edu.az>

facebook: [Journal Of Baku Engineering University](#)

Copyright © Baku Engineering University

ISSN 2521-6368

ISSN 2521-6368



Journal of Baku Engineering University

PHYSICS

Baku - AZERBAIJAN

Journal of Baku Engineering University

PHYSICS

2024. Volume 8, Number 2

CONTENTS

MORPHOLOGY OF CRYSTAL GROWTH DURING II\leftrightarrowI PHASE TRANSFORMATION IN $K_{0.945}Rb_{0.055}NO_3$ MONOCRYSTAL	
<i>R.B.Bairamli, E. V. Nasirov, U.S. Abdurahmanova, U.F. Bairamli, V.I.Nasirov</i>	55
SPATIAL STRUCTURES OF [ILE3]-AND [PHE3]-RUBISCOLIN-5 MOLECULE ANALOGUES	
<i>Niftali Godjajev, Leyla Agayeva, Yasaman Karimli</i>	62
IMPACT OF SULFUR ION CONCENTRATION ON THE OPTICAL AND STRUCTURAL CHARACTERISTICS OF Ag-Ag₂S Core-Shell NANOSTRUCTURES	
<i>Fatma Ismayilova, Mustafa Muradov, Mahammad Baghir Baghirov, Goncha Eyvazova, Sevinj Mammadyarova</i>	74
GALVANOMAGNETIC PROPERTIES OF $Gd_xSn_{1-x}Se$ SOLID SOLUTIONS	
<i>O.M.Hasanov, C.I.Huseynov, H.A.Aslanov, X.A.Adgozalova, G.A.Garashova, R.B.Bayramli</i>	81
SUMMARY OF EXPERIMENTAL DATA ON THE DENSITY AND VISCOSITY OF "ILISU SANGAR" AND "ILISU BESHBULAG" THERMAL WATERS IN THE GAKH DISTRICT OF AZERBAIJAN	
<i>M.M. Bashirov, N.D. Nabiyev, N.S.Rzayev, A.N. Namazovav</i>	91
SPATIAL STRUCTURES OF THE N-TERMINAL ANALOGUES OF NOCICEPTIN MOLECULE	
<i>Larisa Ismailova, Simnara Akhmedova, Namiq Akhmedov</i>	97

UOT: 621.315.592

PACS: 61.05.-a

PACS: 65.40.-B

DOI: <https://doi.org/10.30546/09081.2024.102.6098>

MORPHOLOGY OF CRYSTAL GROWTH DURING II \leftrightarrow I PHASE TRANSFORMATION IN $K_{0.945}Rb_{0.055}NO_3$ MONOCRYSTAL

R.B.BAYRAMLI¹, E. V. NASIROV² U.S. ABDURAHMANOVA¹, U.F. BAYRAMLI³, V.I.NASIROV^{2,4}¹Baku Engineering University²Azerbaijan Military Institute named after Heydar Aliyev³National Defence University, Baku Military College⁴Azerbaijan State Pedagogical University

Baku / AZERBAIJAN

rabayramov@beu.edu.az, uabdurahmanova@beu.edu.az

ARTICLE INFO	ABSTRACT
<p>Article history:</p> <p>Received: 2024-12-08</p> <p>Received in revised form: 2025-01-13</p> <p>Accepted: 2025-01-16</p> <p>Available online</p> <hr/> <p>Keywords:</p> <p>monocrystal, phase transformation, rhombohedral modification</p>	<p>$K_{0.945}Rb_{0.055}NO_3$ monocrystals were grown from aqueous solutions of KNO_3 and $RbNO_3$ by isothermal crystallization method and the morphology of crystal growth during II\leftrightarrowI phase transformations in these crystals was studied by optical microscopy. It was determined that two polymorphic transformations occur in the studied crystal from room temperature to the melting temperature. The structural transformations in these crystals are enantiotropic and of the monocrystal-monocrystal type. The equilibrium temperature between the interconverting II and I modifications is $T=455\pm 0.5K$.</p> <p>In the investigated sample, a repeated II\rightarrowI phase transformation was studied, and the growth of the process was observed in a mono-nucleated manner in the [001] crystallographic direction. This transformation was accompanied by the movement of the non-linear boundary separating the phases.</p> <p>The transformation rate is as $\llbracket 2 - v_{[001]} > 1 - v_{[001]} \rrbracket$. Experiments show that the rhombohedral modification existing between modifications I and II in potassium nitrate is not detected in the studied sample. Partial replacement of K^+ ions with Rb^+ ions increases the equilibrium temperature between modifications II and I by about 55 K.</p>

1. Introduction

The study of polymorphous transformations in nitrate compounds of alkali metals is of scientific and practical interest. Due to their high piezoelectric and ferroelectric properties, the technological capabilities of the compounds create great opportunities for their use as active elements (KNO_3 -III phase ferroelectric) in electronic devices (capacitors) [1, 2].

In addition, these compounds are strong oxidizing agents used in pyrotechnics, metallurgy, analytical chemistry and the preparation of pharmaceutical preparations [3]. Potassium salts are used in the production of conversion devices, memory elements and radiation heat transfer devices [4].

To study the mechanism of polymorphic transformations, it is necessary to study the morphology of new crystal growth during these transformations, the crystallographic directional relationships between the mutual transformation modifications, as well as the kinetics of the

process. In this regard, it is convenient to use optically transparent crystals as a research object [5]. Nitrate compounds of alkali metals are such substances, and numerous research works have been devoted to the study of structural transformations in them, and a summary of the results obtained is given in [6].

This research work is devoted to the study of the regularities of polymorphic transformations in the $K_{0,945}Rb_{0,055}NO_3$ crystal obtained as a result of partial replacement of K^+ ions with Rb^+ ions in KNO_3 crystals. Polymorphic transformations in this compound have not been studied previously.

Potassium nitrate exists in three different polymorphic forms at atmospheric pressure [7].

At ~ 299 K, phase II, α - KNO_3 has a rhombic (aragonitic) structure with lattice parameters $a=5,414$ Å, $b=9,164$ Å and $c=6,431$ Å, space group Pmcn [8, 9].

At temperatures $T > 403$ K, phase I, β - KNO_3 , transforms into a rhombohedral (calcite) structure with lattice parameters $a=5,42$ Å and $c=19,41$ Å and space group R-3m [10]. On the other hand, during cooling, phase I first transforms into phase III (ferroelectric phase) at ~ 397 K, and then phase III transforms into phase II at ~ 383 K (γ - KNO_3 , rhombohedral structure with lattice parameters $a=5,43$ Å and $c=9,112$ Å, space group R-3m) [9, 10]. It has been determined that the temperature range corresponding to phase III expands at high pressure, and that phase III also appears upon heating and belongs to the space group R3m [11].

In rubidium nitrate four polymorphic transformations occur between room temperature and melting temperature. At a temperature of ~ 298 K, phase IV has a trigonal lattice with lattice parameters $a=10,479$ Å, $c=7,452$ Å, and space group R3m [12-14]. At $T > 437$ K, phase IV transforms into a cubic crystal III with lattice parameters $a=4,36$ Å, and space group Pm-3m [14]. At $T > 492$ K, the III \rightarrow II transformation occurs and the cubic lattice transforms into a hexagonal lattice with lattice parameters $a=5,48$ Å, $c=10,71$ Å, and a space group of R-3m [16]. At $T > 564$ K, modification II transforms into cubic modification I with lattice parameters $a=7,32$ Å, and space group Fm-3m [16].

2. Experimental part

The $K_{0,945}Rb_{0,055}NO_3$ crystals were obtained by isothermal crystallization from aqueous solutions of KNO_3 and $RbNO_3$ at room temperature. To achieve the perfection and purity of the obtained samples, potassium nitrate of the "CDA" brand and rubidium nitrate of the "XC" brand were subjected to multiple crystallizations.

For conducting research using an optical microscope, samples with dimensions of $1 \times 0,5 \times 5$ mm were used. Because these measurements are suitable for conducting related studies, i.e. for observation under a microscope (figure 1).

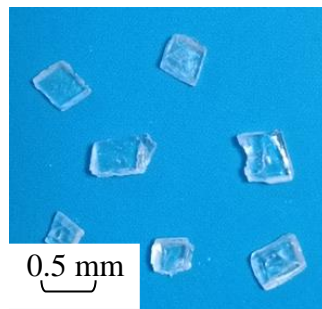


Figure 1. $K_{0,945}Rb_{0,055}NO_3$ monocrystals obtained from aqueous solution

In general, the samples were obtained in the form of flat plates and needlelike. The length of the needles was in the crystallographic direction [001]. The experiments were carried out on a MIN-8 polarization microscope equipped with a heater using a “Levenhuk C310 NK” type camera. Using a computer crystal growth was observed during polymorphic transformations [17, 18]. The temperature of the crystal was measured using a thermocouple touching it. The error of the temperature measurements was $\pm 0,5^{\circ}C$ at $100^{\circ}C$. Temperature fluctuations should be minimal.

Temperature stability is important to prevent possible defects in the crystal.

During the morphological studies of the sample, first of all, the equilibrium temperature between modifications II and I was determined as $T_0=(455\pm 0,5)$ K. In the $K_{0.945}Rb_{0.055}NO_3$ crystal, the II → I transformation occurs at a temperature $T_{tr} > T_0$, with the formation of a nucleus of a modification I crystal within a modification II crystal and its growth mainly in the [100] crystallographic direction (Fig. 2.b). Here T_{tr} is the transformation temperature, and T_0 is the equilibrium temperature between the phases.

Polymorphic transformations always occur at temperatures $T_{tr} > T_0$ and the temperature difference $\Delta T = T_{tr} - T_0$ depends on the perfection of the parent crystal [6,19].

Experiments show that in the considered case the delay of transformation between modifications II and I is $\Delta T \sim 2K$.

As can be seen from Fig. 2.b, after the formation of the I-phase nucleus, it grows rapidly in the [100] direction within the parent crystal and after the growth in this direction is completed, it continues in both directions in the [001] crystallographic direction (Fig. 2. c-e). The growing nucleus is shown in the figure by an arrow. The growth rate in both directions is $v_{[100]} > v_{[001]}$. After complete transformation, I modification crystal is obtained (Fig. 2.f). It showed that no further morphological changes occurred in the crystal under study until the melting temperature of the crystal.

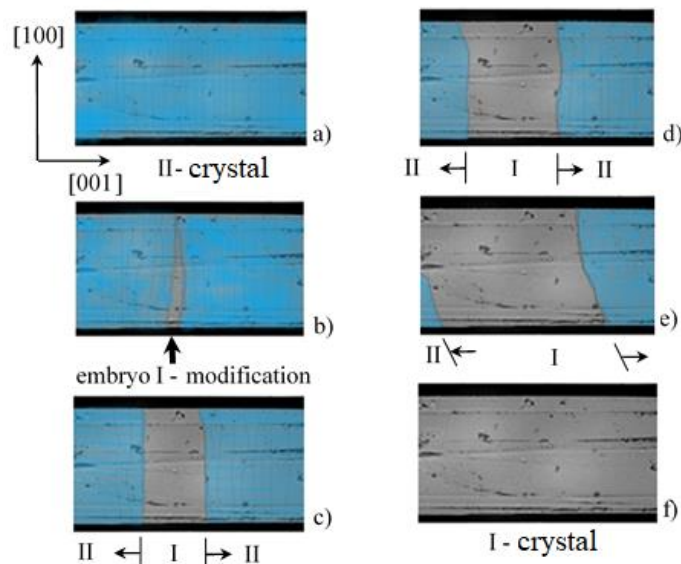


Figure 2. Formation and growth of the nucleus of the I modification ($T=455$ K) crystal inside the II modification crystal during the II → I phase transformation in the $K_{0.945}Rb_{0.055}NO_3$ crystal. a- II crystal, b- formation of the I crystal nucleus inside the II crystal and its rapid growth in the [100] direction, c-e- growth of the I crystal nucleus in both directions in the [001] direction, f- I crystal after the complete II → I phase transformation (magnification $\times 90$).

When the I-modification crystal is cooled to a temperature of 453K, the reverse transformation, that is, the I→II transformation, occurs at a temperature of $T_{tr} < T_0$. This process also occurs with the formation and growth of a II phase crystal nucleus within the I phase (Figure 3. a).

It was determined that during the experiments the boundary line separating the phases bent at an angle of 45° . This bending can be explained by the stress generated within the crystal during the phase transformation. After the reverse transformation was completed, the relatively low defect content of the II-modification crystal (Fig. 3.f) led to the observation of a repeated II→I transformation in the same sample. X-ray studies also showed that after the II-I-II transformation, the crystal completely restored its original state.

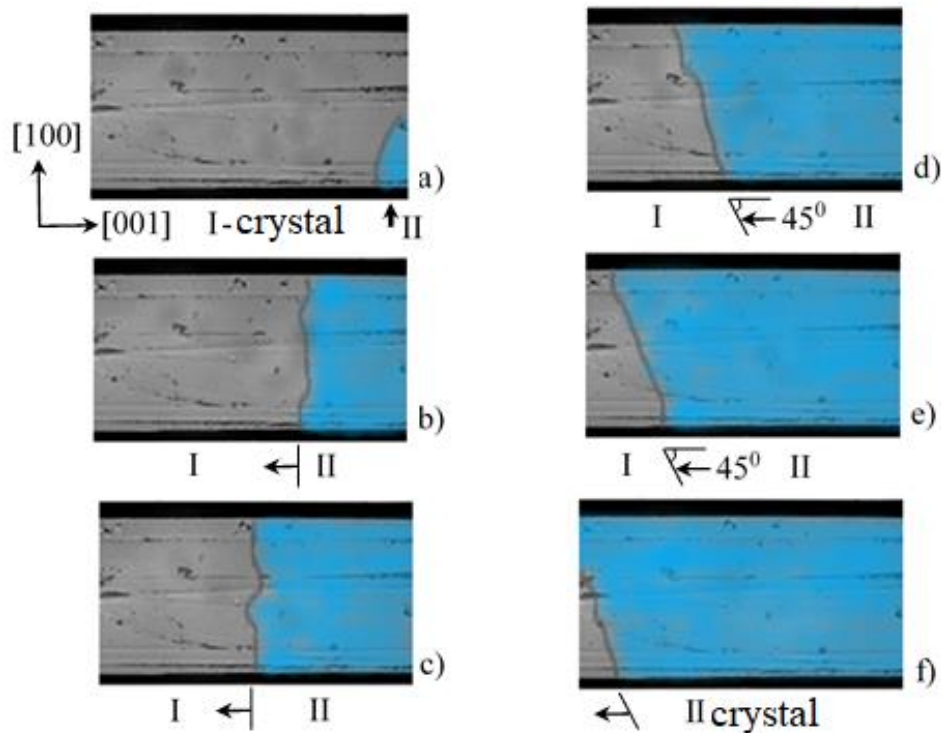


Figure 3. Formation and growth of the nucleus of the II modification ($T=453K$) crystal inside the I modification crystal during the I→II phase transformation in the $K_{0.945}Rb_{0.055}NO_3$ crystal. a- formation of the II crystal nucleus inside the I crystal and its rapid growth in the [100] direction, b-c- rapid growth of the II crystal nucleus in the [001] direction, d-e- 45° bending of the boundary and rapid growth of the II crystal nucleus in the [001] direction, f- II crystal after the complete I→II phase transformation (magnification $\times 90$).

The II→I phase transformation was again carried out in the investigated sample and the equilibrium temperature was determined. In this case, the transformation temperature in the crystal was not different as in the first transformation, the process occurred in the [001] direction and was mono embryonic (Fig. 4. b-d). The straightness of the boundary between the II and I phases is not preserved (Fig. 4.c, e,j), the transformation rate is $\llbracket 2 - v_{[001]} > 1 - v_{[001]} \rrbracket$. Experiments conducted on $K_{0.945}Rb_{0.055}NO_3$ samples show that the rhombohedral modification existing between modifications I and II in potassium nitrate is not detected in this case.

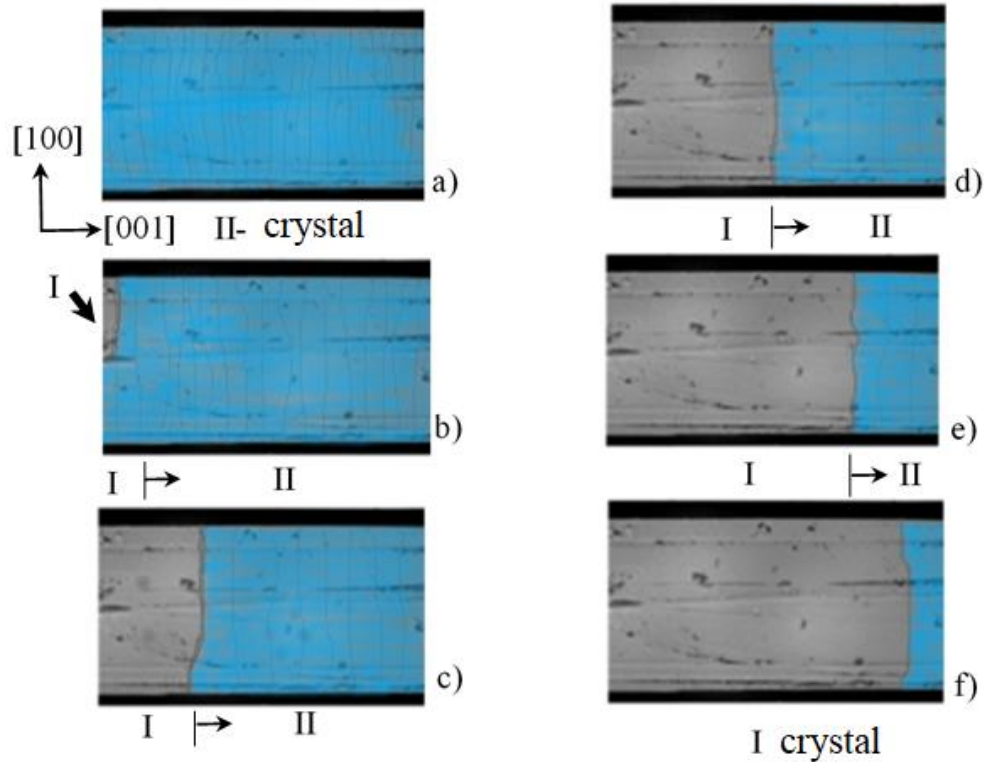


Figure 4. Formation and growth of the nucleus of the I modification ($T=455$ K) crystal within the II modification crystal during the second II \rightarrow I phase transformation in the $K_{0.945}Rb_{0.055}NO_3$ crystal. a- II crystal formation of microcracks on the crystal surface (gray lines), b- formation of the I crystal nucleus within the II crystal and its rapid growth in the [100] direction, c-d-e- rapid growth of the I crystal nucleus in the [001] direction, reduction of microcracks, f- I crystal after complete II \rightarrow I phase transformation (magnification $\times 90$).

3. Conclusion

It has been experimentally determined that polymorphic transformations in the $K_{0.945}Rb_{0.055}NO_3$ crystal are enantiotropic in nature, are of the monocrystal-monocrystal type. During II \leftrightarrow I transformations the growth of crystals of modifications I and II occurs through the formation and growth of a crystal nucleus within the parent crystal.

It was also determined that there is no intermediate modification between modifications I and II. The rhythmic growth observed in potassium nitrate crystals during the II \rightarrow I transformation [19, 20] is not detected in this case.

In the studied sample, a repeated II \rightarrow I polymorph transformation was carried out, and between the temperatures of the first transformation and the second transformation any difference was not observed. It was determined that the process was monoemrionic and the growth proceeded mainly in the [001] direction. Partial replacement of K^+ ions with Rb^+ ions in potassium nitrate between modifications II and I increases the equilibrium temperature by about 55 K. This suggests that the phase transitions of mixed phases make these materials suitable for use in highly sensitive sensors. At the same time, their high heat capacity and stable phases make them suitable for thermal storage systems. Mixed nitrates are more stable and powerful combustible materials, and their crystals have high dielectric constants, making them suitable for capacitors and microelectronics.

REFERENCES

1. Kumar, N. and Natha, R., (2010) Ferroelectric properties of potassium nitrate-polymer composite films // J. Pure Appl. & Ind. Phys. v.1, (1), pp. 21-35.
<https://www.scribd.com/document/248302128/PHSV01I01P0021-pdf>
2. Erdinc, B. and Akkus, H., (2010) Ab-initio study of the electronic structure and optical properties of KNO₃ in the ferroelectric phase // Phys. Scr. v. 79, pp. 025601-025006, 2009.
<https://doi.org/10.1088/0031-8949/79/02/025601>.
3. Venkatesh. E., Naresh V. and Rajesh N. (2022) Propulsion of rocket using potassium nitrate // International Journal of Engineering Inventions (IJEI) v. 11, 9. pp. 01-07
<https://www.ijejournal.com/v11-i9.html>
4. Tesleva E.P. (2006) "Study of polymorphic transformations in ion-molecular dielectrics by methods of physical acoustics and thermal physics", Ph. D. Thesis. Tomsk University Kazan. 187 p.
<https://www.dissercat.com/>
5. Kitaigorodskii A. I., Mnyukh Yu.V., Asadov Y.G. (1965) Relationships for single crystal growth during polymorphic transformation // Journal of Physics and Chemistry of Solids. v. 26, (3), pp. 463-464.
[https://doi.org/10.1016/0022-3697\(65\)90120-4](https://doi.org/10.1016/0022-3697(65)90120-4)
6. Nasirov V.I. (1997) Polymorphism in optically transparent crystals. Baku, 166 p.
7. Adiwidjaja G., Pohl D. Superstructure of α -phase of potassium nitrate // Acta Cryst. C59: i139–i140, 2003,
<https://doi.org/10.1107/S0108270103025277>
8. C.N.R. Rao, B. Prakash, M. Natarajan. (1975.) // Washington: National Standard Reference Data System-National Bureau of Standards. p. 48.
<https://nvlpubs.nist.gov/nistpubs/Legacy/NSRDS/nbsnsrds53.pdf>
9. Nimmo J.K., Lucas B.W. (1973) A neutron diffraction determination of the crystal structure of α -phase potassium nitrate at 25°C and 100°C // J. Phys. C: Solid State Phys. v. 6, (1), pp. 201-211
<https://iopscience.iop.org/article/10.1088/0022-3719/6/2/001>
10. Nimmo J.K., Lucas B.W., (1976) The crystal structures of γ - and β -KNO₃ and the α - γ - β phase transformations // Acta Cryst., B32, pp. 1968–1971
<https://doi.org/10.1107/S0567740876006894>
11. Sawada S, Nomura S. and Fuji S. (1958) Ferroelectricity in the Phase III of KNO₃ // J. Phys. Soc. Japan, v.13, p. 1549.
<https://doi.org/10.1143/JPSJ.13.1549>
12. Pohl J., Pohl D. And Adiwidjaja. G. (1992) Phase transition in rubidium nitrate at 346 K and structure at 296, 372, 413 and 437 K // Acta Cryst. B.48. PP. 160-166.
<https://doi.org/10.1107/S0108768191013459>
13. Shamsuzzoha M., Lucas B.W. (1982) Structure (neutron) of phase-IV rubidium nitrate at 298 K and 403 K // Acta Cryst B.38, pp. 2353–2357
<https://www.academia.edu/upload/document>
14. Liu J.J., Duan C.G., Ossowski M.M., Mei W.N., Smith R.W. and Hardy J.R. (2001) Molecular Dynamics of Structural Phase Transitions in RbNO₃ and CsNO₃ // J. Solid State Chem. v. 160, pp. 222-229.
<https://doi.org/10.1006/jssc.2001.9226>
15. Shinnaka Y., Yamamoto S. (1981) X-Ray Study of Orientational Disorder in Cubic RbNO₃ // Journal of the Physical Society of Japn. v. 50, (6), pp. 2091-2094
<https://doi.org/10.1143/JPSJ.50.2091>
16. Ahtee M., Hewat A. W. (1980) Structures of the High Temperature Phases of Rubidium Nitrate // Physica Status Solidi. v. 58, 2, pp. 525-531
<https://doi.org/10.1002/pssa.2210580224>
17. Asadov Yu.G., Nasirov V.I., Bairamov R.B, Nasirov E.V. (2021) A method of studying the mechanism of structure transformations in optically transparent crystals // Patent No. İ 2021 0093.
<http://dx.doi.org/https://patent.copat.gov.az/fi>

18. Nasirov V.İ., Bairamov R.B., Asadov Y.G., Haziyeva A.F. (, 2014) Single crystal↔single crystal polymorphic transformations in $K_{0.985}Rb_{0.015}NO_3$ // Crystallogr. Reports. v. 59. pp. 1121-1126.
<http://dx.doi.org/10.1134/S1063774514070165>
19. Nasirov V.İ., Bairamov R.B., Nasirov E.V. (2015) Morphology and kinetics of polymorphic transformations in $K_{0.965}Rb_{0.035}NO_3$ single crystals // Crystallogr. Reports. v. 60. pp. 1155-1159.
<https://doi.org/10.1134/S1063774515070184>
20. Nasirov V.İ., Bairamov R.B., Nasirov E.V. (2017) Investigation of $K_{0.965}Cs_{0.035}NO_3$ Crystal Using X-Ray and Optical Microscopic Methods // Journal of Baku Engineering University Physics v. 1. pp. 186-198.
https://physics.beu.edu.az/archives/physics_2017_2.pdf

UOT: 577.32

PACS: 11.15.-p

DOI: <https://doi.org/10.30546/09081.2024.102.7075>

SPATIAL STRUCTURES OF [ILE3]-AND [PHE3]- RUBISCOLIN-5 MOLECULE ANALOGUES

Niftali GODJAYEV, Leyla AGAYEVA, Yasaman KARIMLI

Baku State University

leylanamig@mail.ru

ARTICLE INFO	ABSTRACT
<p>Article history:</p> <p>Received: 2025-01-12</p> <p>Received in revised form: 2025-01-13</p> <p>Accepted: 2025-01-16</p> <p>Available online</p> <p>Keywords:</p> <p>nutrients, opioid, rubiscolin, spatial structure, conformation.</p>	<p>Rubiscolin molecules belong to the class of opioids derived from food substances. To understand the various physiological functions they perform, to target them purposefully, and to synthesize artificial analogs that perform specific functions of the natural molecule, it is necessary to study their three-dimensional spatial structures. The spatial structures of rubiscolin molecules and their analogs were investigated using theoretical conformational analysis methods. The potential energy of the molecule was chosen as the sum of non-valent, electrostatic, torsion interaction energies and hydrogen bond energies. The spatial structures of [Ile3]- and [Phe3]-rubiscolin-5 molecules were studied in the context of the low-energy conformations of the natural rubiscolin molecule. The calculations revealed that the solid structure of both analogs is represented by eight low-energy conformations, similar to those of the natural rubiscolin-5 molecule. It has been shown that the energy and geometric parameters of the molecules in both analogues are the same as in the natural rubiscolin-5 molecule, therefore it is not advisable to propose to synthesize both artificial analogues.</p>

Introduction

Regulatory peptides, first discovered in the second half of the 20th century, are actively studied by both physiologists and pharmacologists, since the area of biological activity of peptides is extremely wide. They are one of the main links that unite the three regulatory systems of the body - the nervous system, endocrine and immune into a single whole. At present, more than 9000 physiologically active peptides have been characterized in various animal species and in humans. These are short chains of amino acids (2-70 residues) that act as signal molecules. Most of these peptides cannot be confidently attributed to either neurotransmitters or hormones, since they are synthesized both by neurons (transmitting a signal at the synapse level) and by cells of peripheral tissues (transmitting a signal over longer distances, like hormones). Regulatory peptides are characterized by the impact on many systems of the body at once. Opioid peptides are currently considered the most studied group of peptides signaling substances. Opium causes pain relief, sedation and falling asleep, as well as a euphoric state and a number of vegetative reactions. Opioid peptides are of animal and plant origin. A number of exogenous peptides obtained from food have opiate-like properties. These peptides were called exorphins. The discovery of the opioid activity of the peptide components of food led to the assumption that certain types of food can act on the central nervous system like opiate drugs. Exorphins have been isolated from various plant species. Rubiscolins -5 and -6 are also of

great interest to scientists. These peptides have affinity mainly for β -receptors. Rubiscolins were first isolated from spinach leaves. However, the degree of homology of the large RUBISCO subunit in different species of higher plants is extremely high (more than 90%), and the content of RUBISCO in green leaves is up to 50% of the total protein. Therefore, rubiscolins in significant amounts can enter the body when consuming not only spinach, but also lettuce, sorrel, pars-ley, etc. The green leaves of these plants are an important component of a balanced diet, so studies of the possible neurotropic effect of rubiscolins are of practical value [1-6].

Materials and methods

We have studied the structural and functional organizations of opioid peptides enkephalins, endorphins, endomorphins, dynorphins, neoendorphins, adrenorphin, and are currently studying the spatial structure of exorphins, casomorphins, lactoferroxins, casoxins, soymorphins, rubiscolins. This work is a continuation of our previous studies [7-15].

The molecule was calculated using the method of theoretical conformational analysis. The potential function of the system is chosen as the sum of nonvalent, electrostatic and torsional interactions and the energy of hydrogen bonds. Non-valent interactions were assessed using the Lennard-Jones potential. Electrostatic interactions were calculated in the monopole approximation according to Coulomb's law using partial charges on atoms. The conformational capabilities of the rubiscolin molecule were studied in an aqueous environment, and therefore the dielectric constant was taken to be 10. The energy of hydrogen bonds was estimated using the Morse potential. Our above-mentioned works detail the potential features used. When presenting the calculation results, a classification of peptide structures according to conformations, main chain shapes, and peptide backbone shapes was used. Conformational states are completely determined by the values of the dihedral angles of the main and side chains of all amino acid residues included in a given molecule. The backbone forms of a fragment are formed by combinations of the forms of R, B, L residues in a given sequence. The forms of the dipeptide backbone can be divided into two classes - folded (f) and unfolded (e) forms, which are called shapes. All conformations are grouped by main chain shapes, and shapes by shapes. To designate the conformational states of residues, identifiers of the X_{ij} type are used, where X defines the low-energy regions of the conformational map and $ij...=11...,12...,13...,21...$ determines the position of the side chain, with index 1 corresponding to the angle value ranging from 0 to 120°, 2 – from 120° to -120°, and 3 – from -120° to 0°. Designations and readings of rotation angles correspond to the IUPAC-IUB nomenclature [16]. To calculate the spatial structure of peptide molecules was used a program developed by N.M.Gojayev and his staff [17].

Results and Discussion

In [18] we studied the three-dimensional structure of the rubiscolin-5 molecule (Tyr1-Pro2-Leu3-Asp4-Leu5-NH2) based on low-energy conformations of the corresponding amino acid residues and determined its stable conformations. The calculation results showed that there is an energy differentiation between the conformations, forms of the main chains and shapes. The conformations of eight shapes fall within a wide energy range of 0-5.0 kcal/mol. The most stable conformations were selected from each shape and are presented in Table 1. The energy contributions of non-valent (U_{nv}), electrostatic (U_{el}), torsional (U_{tors}) interactions and the relative (U_{rel}) energy of the optimal conformations of the rubiscolin-5 molecule are indicated here. The energy of non-valent interactions in low-energy conformations changes in the energy range (-22.3) - (-18.9) kcal/mol, electrostatic interactions (-4.6) - (0.9) kcal/mol, torsional interactions (2.9-

5.6) kcal/mol. The geometric parameters of four conformations whose relative energy is less than 4.0 kcal/mol are presented in Table 2.

Table 1. Optimum conformations of the rubiscoline-5 molecule, their shapes, the shapes of their main chains, the energy contribution of non-valent, electrostatic, torsion interactions and relative energies.

№	Shapes	CONFORMATION	Energy contribution			U _{rel}
			U _{nv}	U _{el}	U _{tors}	
1	efee	B ₃ RB ₂₁ B ₃ B ₃₂	-20.0	-4.6	3.7	0
2	efff	B ₃ RR ₁₂ R ₁ R ₂₁	-22.3	-3.8	5.6	0.4
3	efef	B ₃ RB ₃₁ R ₃ R ₂₁	-21.3	-3.7	4.3	0.2
4	eeef	B ₂ BB ₂₁ R ₁ R ₂₁	-20.3	0.5	3.0	4.0
5	effe	B ₃ RR ₂₁ B ₃ B ₃₂	-18.9	-0.7	3.0	4.3
6	eefe	B ₁ BR ₃₂ B ₁ B ₃₂	-21.7	1.0	4.8	4.9
7	eeff	B ₁ BR ₂₃ R ₃ R ₃₂	-19.8	0.9	2.9	5.0
8	eeee	B ₁ BB ₂₁ B ₁ B ₃₂	-19.8	0.9	3.1	5.0

Table 2. Geometric parameters (in degrees) of low energy conformations of the molecule rubiscolin-5 (the values of the dihedral angles are given in the sequence $\varphi, \psi, \omega, \chi^1, \chi^2...$)

Residue	B ₃ RB ₂₁ B ₃ B ₃₂	B ₃ RR ₁₂ R ₁ R ₂₁	B ₃ RB ₃₁ R ₃ R ₂₁	B ₂ BB ₂₁ R ₁ R ₂₁
Tyr1	-95 159 168 -71 104 0	-89 158 176 -73 113 0	-65 155 171 -70 107 0	-71 115 170 171 79 0
Pro2	-60 -46 167	-60 -33 -179	-60 -63 169	-60 120 -173
Leu3	-122 118 174 173 61 180 177	-66 -41 -177 65 98 179 -179	-106 62 180 -75 65 179 180	-108 103 175 173 62 179 -172
Asp4	-107 144 -175 60 90	-81 -31 176 61 85	-76 -49 179 -56 89	-99 -46 180 55 107
Leu5	-118 119 180 -54 175 -175 180	-63 -45 179 176 63 179 176	-77 -52 180 176 62 179 175	-116 -68 180 175 62 179 176
ΔU	0	0.4	0.2	4.0

Rubiscolin-5 and various analogues of Rubiscolin-5 molecules were synthesized by Sobolczyk M., Perlikowska R. The spatial structure of the [Ile3]-rubiscolin-5 and [Phe3]-rubiscolin-5 molecules synthesized by them was studied. The spatial structure of the [Ile3]-rubiscolin-5 molecule was calculated based on the low-energy conformations of the natural rubiscolin-5 molecule shown in Table 1. At this time, nine conformations of the side chain of the Ile amino acid residue in each low-energy form of the natural molecule, which are possible according to the torsion potential, were considered. The results of the calculations show that there is differentiation according to the energies of the conformations, but there is no differentiation according to the shapes of the main chain forms. Among the calculated conformations, the lowest-energy conformation of the side chain of the Ile amino acid residue in the eight low-energy forms of the main chain was selected. These conformations, their contributions to them by non-valent, electrostatic, and torsional interaction energies, and their total and relative energies are shown in Table 3. As can be seen from Table 3, their relative energies vary in the range of (0 – 6.4) kcal/mol. A comparison of Tables 1 and 3 shows that all low-energy structures of the natural molecule remain the same as low-energy for the [Ile3] analogue.

Table 3. Optimum conformations of the [Ile3]- rubiscolin-5 molecule, their shapes, the shapes of their main chains, the energy contribution of non-valent, electrostatic, torsion interactions, the total and relative energies.

№	Shapes	CONFORMATION	Energy contribution			U _{tot}	U _{rel}
			U _{nv}	U _{el}	U _{tors}		
1	efee	B ₃ R B ₂₁ B ₃ B ₃₂	-18.9	4.4	4.2	-19.2	0.3
2	efff	B ₃ R R ₃₂ R ₁ R ₁₂	-19.2	-3.7	3.3	-19.5	0
3	efef	B ₃ R B ₂₁ R ₃ R ₂₁	-19.6	-3.9	4.4	-19.1	0.4
4	eeef	B ₂ B B ₃₂ R ₁ R ₂₁	-21.5	0.4	4.4	-16.7	2.8
5	effe	B ₃ R R ₃₂ B ₃ B ₃₂	-17.8	-0.3	3.1	-15.0	4.5
6	eeefe	B ₁ B R ₃₃ B ₁ B ₃₂	-19.1	1.2	4.8	-13.1	6.4
7	eeff	B ₁ B R ₃₂ R ₃ R ₃₂	-19.3	1.2	2.8	-15.3	4.2
8	eeee	B ₁ B B ₂₂ B ₁ B ₃₂	-20.3	1.1	3.9	-15.4	4.1

Table 4. Energy inside and between residual interactions in the conformations of the molecule [Ile3]- rubiscolin-5 B₃R B₂₁B₃B₃₂ (U_{rel}=0.3 kcal/mol, first line), B₃R R₃₂R₁R₁₂ (U_{rel}=0 kcal/mol, second line), B₃R B₂₁R₃R₂₁ (U_{rel}=0.4 kcal/mol, third line), B₂B B₃₂R₁R₂₁ (U_{rel}=2.8 kcal/mol, fourth line)

Tyr1	Pro2	Ile3	Asp4	Leu5	
3.3	-3.8	-1.8	-10.9	-2.4	Tyr1
3.7	-4.2	-2.9	-12.3	0.3	
2.1	-4.4	-2.4	-12.3	-0.8	
2.6	-5.7	-4.1	-4.7	-0.7	
	0.1	-0.8	-1.0	-2.2	Pro2
	0.2	-1.8	-0.5	0	
	0.3	-1.9	-0.5	0	
	0.3	-1.1	-0.6	-0.1	
		1.4	-0.6	-1.3	Ile3
		1.6	-1.8	-2.7	
		2.4	-1.6	-2.7	
		0.4	-0.9	-2.5	
			2.0	-1.1	Asp4
			2.5	-1.6	
			2.3	-1.3	
			1.8	-1.4	
				-3.6	Leu5
				-3.6	
				-3.4	
				-4.3	

The relative energies of the first four low-energy conformations in Table 1 vary in the range of (0 – 2.8) kcal/mol. In the eight low-energy conformations shown in Table 3, the contributions to the non-valent interaction energy vary in the range of (-21.5) – (-17.8) kcal/mol, the electrostatic interaction energy in the range of (-4.4) – (1.2) kcal/mol, and the torsion interaction energy in the range of (2.8) – (4.8) kcal/mol (Table 3). The interaction forces between and within amino acid residues in these conformations are shown in Table 4, the values of their dihedral angles are shown in Table 5, and the spatial arrangement of atoms in these conformations is shown in Figure 1. The most stable conformation of the [Ile3]-rubiscolin-5 analogue is B₃R R₃₂R₁R₁₂, which belongs to the efff shape. The relative energy of this conformation in the natural rubiscolin-5 molecule is 0.4 kcal/mol. The conformation is favorable in terms of both non-valent and electrostatic interaction energies. In this conformation, the N- and C- sides of the molecule approach each other, and a hydrogen bond is formed between the H-atom on the N-side of Tyr1

and the C=O atom in the side chain of Asp4 and the N – H atom of the main chain of Leu5, contributing (-2.0) kcal/mol to the total energy. An effective interaction occurs between the positively charged N-side of the molecule and the negatively charged side chain of Asp4, contributing (-12.3) kcal/mol to the total energy (table 4). Tyr1 interacts favorably with the following Pro2-Ile3 dipeptide fragment, contributing (-7.1) kcal/mol to the total energy. Ile3 interacts effectively with the C-side dipeptide fragment, contributing (-4.5) kcal/mol to the total energy (table 4). A comparison of the energy and geometric parameters of the B₃ R R₃₂ R₁ R₁₂ conformation in the [Ile3]-rubiscolin-5 analogue and the native molecule shows that the contribution of different interaction energies to the stabilization of both molecules, the interaction energies between amino acid residues, and the values of the dihedral rotation angles almost coincide (tables 1 and 3, tables 2 and 5).

Table 5. Geometric parameters (in degrees) of low energy conformations of the molecule [Ile3]-rubiscolin-5 (the values of the dihedral angles are given in the sequence $\varphi, \psi, \omega, \chi^1, \chi^2...$)

Residue	B ₃ R B ₂₁ B ₃ B ₃₂	B ₂ R R ₃₂ R ₁ R ₂₁	B ₃ R B ₂₁ R ₃ R ₂₁	B ₂ B B ₃₂ R ₁ R ₂₁
Tyr1	-93 162 167 -73 106 0	-86 157 176 -72 112 0	-63 158 168 -68 108 0	-67 107 165 165 73 0
Pro2	-60 -44 167	-60 -30 -172	-60 -57 169	-60 130 -175
Ile3	-125 119 175 173 179 62 -174	-66 -45 -176 -61 -176 177 -174	-118 101 178 171 174 60 169	-96 104 174 -56 -174 175 -169
Asp4	-104 142 -175 -60 89	-87 -35 -179 61 85	-75 -47 -178 -56 89	-89 -41 178 57 108
Leu5	-118 119 180 -54 172 -175 180	-63 -46 179 176 63 179 176	-40 -56 180 172 62 180 175	-112 -66 179 175 62 179 176
ΔU	0.3	0	0.4	2.8

The second low-energy conformation of the [Ile3]-rubiscolin-5 analog is the B₃ R B₂₁ B₃ B₃₂ of the efee shape, with a relative energy of 0.3 kcal/mol. In the native molecule, its relative energy is 0 kcal/mol (Tables 1 and 3). In this conformation, Pro2, being in the R form of the main chain, turns the tripeptide fragment following it towards the N-side of the molecule. As a result, Tyr1 forms an effective interaction with the tetrapeptide fragment following it Pro2-Ile3-Asp4-Leu5, contributing (-18.9) kcal/mol to the total energy. Electrostatic and non-valent interaction forces play an important role in stabilizing this conformation. The contribution of the electrostatic interaction energy is (-4.4) kcal/mol, which is the largest. The non-valent interaction contributes (-18.9) kcal/mol. Comparisons of Tables 1 and 3, Tables 2 and 5 show that the energy and geometric parameters of the conformations are in perfect agreement.

The third low-energy conformation of the [Ile3]-rubiscolin-5 analog belongs to the B₃ R B₂₁ R₃ R₂₁ effef shape and its relative energy is 0.4 kcal/mol. The relative energy of this conformation in the native molecule is 0.2 kcal/mol. The contribution of the non-valent interaction energy to its stabilization is (-19.6) kcal/mol, and the contribution of the electrostatic interaction energy is (-3.9) kcal/mol. As can be seen, their contributions to the total energy approximately correspond to those of the 1st and 2nd conformations. Here, the unfolded and folded forms of the amino acid residues alternate, and Tyr1 can form effective electrostatic and dispersion interactions with the

tripeptide fragment Pro2-Ile3-Asp4 that follows it. Effective electrostatic interactions form hydrogen bonds between the positively charged N-side of the molecule and the negatively charged side chain of the Asp4 amino acid residue (Table 4). The geometric and energy parameters of the B₃ R B₂₁ R₃ R₂₁ conformation in the analog and in the native molecule are consistent (Tables 1 and 3, Tables 2 and 5)

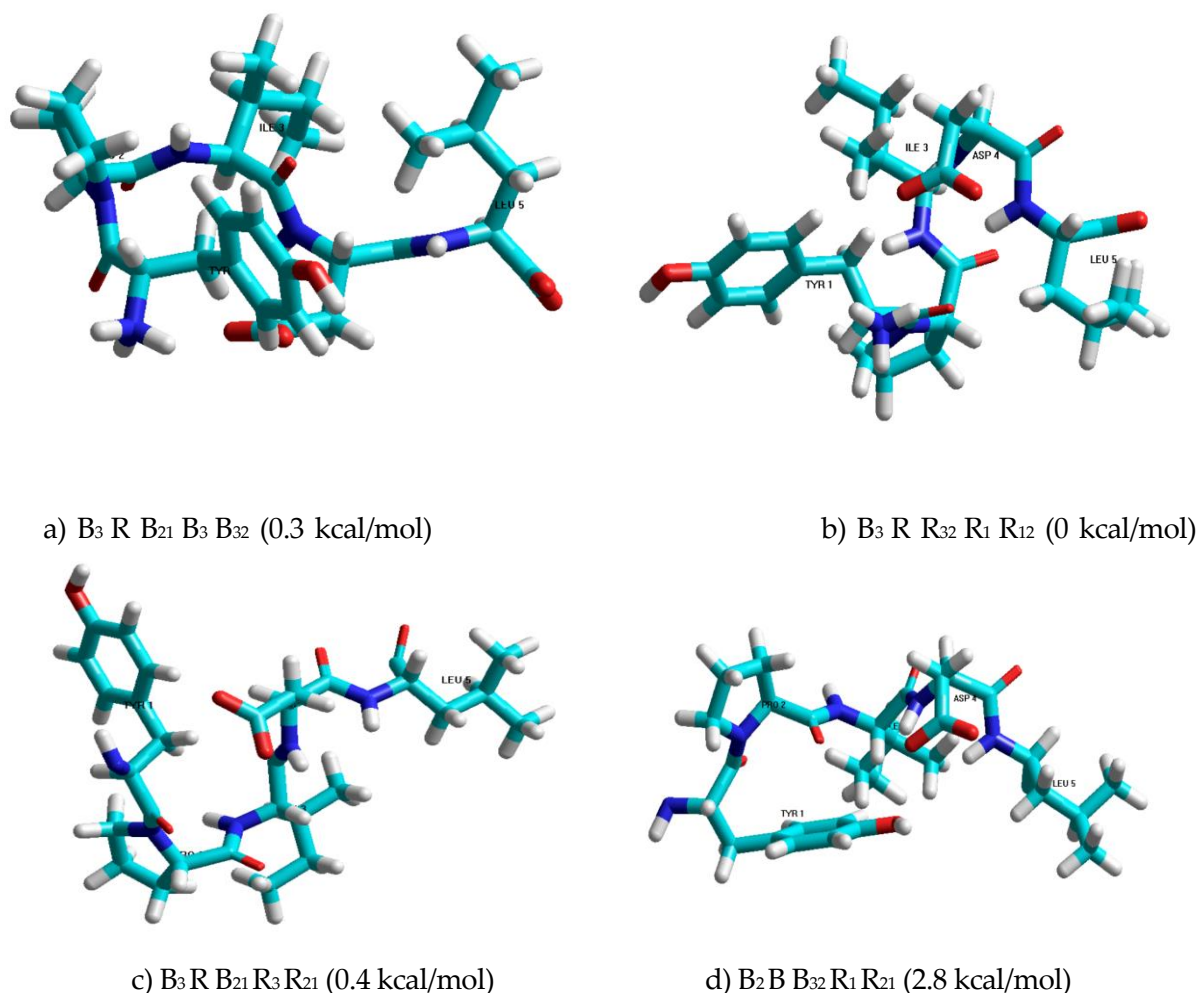


Figure 1. Atomic model of spatial structure of the [Ile3]- rubiscolin-5 molecule a), b), c) and d) corresponded to the structures with the relative energies 0.3 kcal/mol, 0 kcal/mol, 0.4 kcal/mol and 2.8 kcal/mol, respectively.

The relative energy of the B₂ B B₃₂ R₁ R₂₁ conformation of the eeef shape of the [Ile3]-rubiscolin-5 molecule is (2.8) kcal/mol, while its relative energy in the native molecule is 4.0 kcal/mol. The contribution of non-valent interaction energy to this conformation is (-21.5) kcal/mol and is the largest. It is not favorable due to the electrostatic interaction energy, repulsive forces dominate, and their contribution to the total energy is (0.4) kcal/mol (Table 3). The N-side tripeptide fragment of the molecule is in the fully unfolded B B B form of the main chain and distances the positively charged N-side of the molecule from the negatively charged side chain of aspartic acid, and the interaction force between them contributes only (-4.7) kcal/mol to the total energy (Table 4, Figure 1-d). The energy and geometric parameters of this conformation also do not differ from the parameters of the corresponding conformation of the natural molecule.

The relative energies of the low-energy conformations of the efee, eefe, eeff and eeee shapes of the [Ile3]-rubiscolin-5 molecule vary in the energy interval (4.1) – (6.4) kcal/mol. The energies of the low-energy conformations of these shapes vary in the interval (4.3) – (5.0) kcal/mol. In these shapes, the energy and geometric parameters of the natural molecule and the [Ile3]-analogue also correspond.

Based on the above, it can be concluded that the low-energy conformations of the natural Rubiscolin molecule and its [Ile3]-analog are identical. In low-energy conformations, the interactions between amino acid residues, the contributions of different interaction energies to the stabilization of conformations, and the values of dihedral rotation angles are completely consistent. In the natural molecule, the third amino acid residue leucine is replaced by the isoleucine amino acid residue. Both amino acid residues are non-polar. The only difference between them is that the possible region of the isoleucine amino acid residue due to the $\varphi - \psi$ angles is slightly smaller than the possible region of the leucine amino acid residue.

It is known that biomolecules perform their physiological functions in certain spatial structures. Therefore, since the spatial structures of both molecules whose spatial structure is studied are identical, the physiological functions they perform will also be identical. Therefore, it is not appropriate to select the [Ile3]-rubiscolin-5 molecule to synthesize an analog that will perform only certain physiological functions of the natural molecule. In [19], the selection of synthesized analogs of the rubiscolin-5 molecule was based on the spatial structure of the natural molecule.

Table 6. Optimum conformations of the [Phe3]- rubiscoline-5 molecule, their shapes, the shapes of their main chains, the energy contribution of non-valent, electrostatic, torsion interactions, the total and relative energies.

№	Shapes	Conformation	Energy contribution			U _{tot}	U _{rel}
			U _{nv}	U _{el}	U _{tor}		
1	efee	B ₃ R B ₁ B ₃ B ₃₂	-19.6	-4.5	4.1	-19.9	1.0
2	efff	B ₂ R R ₁ R ₁ R ₂₁	-21.6	-3.5	4.3	-20.9	0
3	efef	B ₃ R B ₃ R ₃ R ₂₁	-20.7	-3.7	3.6	-20.9	0
4	eeef	B ₂ B B ₃ R ₁ R ₂₁	-23.1	0.1	4.3	-18.7	2.2
5	eefe	B ₃ R R ₂ B ₃ B ₃₂	-20.4	1.0	2.5	-16.9	4.0
6	eefe	B ₁ B R ₂ B ₁ B ₃₂	-19.4	0.9	3.1	-15.4	5.5
7	eeff	B ₁ B R ₃ R ₃ R ₃₂	-20.7	1.0	4.6	-15.1	5.8
8	eeee	B ₁ B B ₂ B ₁ B ₃₂	-17.9	-0.6	2.8	-15.6	5.3

The [Phe3]-rubiscolin-5 analogue of the rubiscolin-5 molecule was also selected based on the article [19]. The spatial structure of the [Phe3]-rubiscolin-5 analogue was studied based on the low-energy conformations of the natural rubiscolin-5 molecule shown in Table 1. In each low-energy conformation, the χ angle of the Phe side chain, which exists in the 60°, 180° and -60° states according to the torsion potential, was considered. The results of the calculations show that differentiation occurs only according to the conformations of the phenylalanine side chain. The most stable conformation of the Phe side chain was selected, and these conformations, the forms and shapes of the main chain, the contribution of their various interaction energies, total and relative energies are shown in Table 6. The amino acid residues and internal interaction energies in four conformations with relative energies less than 4.0 kcal/mol are shown in Table 7, the

values of their dihedral rotation angles are shown in Table 8, and the spatial arrangement of atoms in these conformations is shown in Figure 2, a, b, c, d.

Table 7. Energy inside and between residual interactions in the conformations of the molecule [Phe3]- rubiscolin-5 B₃R B₁B₃B₃₂ (U_{rel}=1.0 kcal/mol, first line), B₃R R₁R₁R₂₁ (U_{rel}=0 kcal/mol, second line), B₃R B₃R₃R₂₁ (U_{rel}=0.0 kcal/mol, third line), B₂B B₃R₁R₂₁ (U_{rel}=2.2 kcal/mol, fourth line)

Tyr1	Pro2	Phe3	Asp4	Leu5	
-3.8	-4.3	-2.9	-12.2	-0.3	Tyr1
3.4	-2.7	-3.2	-9.6	-2.3	
2.1	-4.4	-2.0	-11.8	-0.2	
2.4	-5.6	-5.2	-5.9	-2.4	
	0.2	-2.2	-0.4	0	Pro2
	0.2	-1.7	-1.1	-2.3	
	0.3	-2.4	-0.6	0	
	0.3	-1.2	-1.1	-0.1	
		0.3	-0.7	-2.6	Phe3
		0.2	-2.2	-1.4	
		-0.1	-0.6	-1.7	
		0.2	-0.4	-0.9	
			2.5	-1.7	Asp4
			2.0	-1.1	
			2.3	-1.7	
			1.8	-1.3	
				-3.6	Leu5
				-3.6	
				-3.8	
				-3.6	

Table 8. Geometric parameters (in degrees) of low energy conformations of the molecule [Phe3]-rubiscolin-5 (the values of the dihedral angles are given in the sequence $\varphi, \psi, \omega, \chi_1, \chi_2, \dots$)

Residue	B ₃ R B ₁ B ₃ B ₃₂	B ₃ R R ₁ R ₁ R ₂₁	B ₃ R B ₃ R ₃ R ₂₁	B ₂ B B ₃ R ₁ R ₂₁
Tyr1	-93 161 167 -72 106 0	-88 157 -173 -74 112 0	-65 155 170 -70 107 0	-66 110 165 165 75 0
Pro2	-60 -46 165	-60 -41 -166	-60 -62 169	-60 129 -171
Phe3	-127 121 178 60 94	-68 -38 -178 65 84	-107 98 180 -60 90	-89 89 -174 -62 94
Asp4	-103 143 -173 -60 90	-85 -34 -179 62 85	-76 -49 179 -56 89	-96 -43 180 57 109
Leu5	-117 119 180 -53 173 -175 180	-63 -45 179 176 63 179 179	-77 -52 180 177 63 179 175	-114 -79 180 -178 62 179 174
ΔU	1.0	0	0	2.2

The relative energies of the low-energy conformations of the [Phe3]-rubiscolin-5 analogue vary in the energy range (0-6.0) kcal/mol (Table 7). The contribution of non-valent interaction energy to these conformations varies in the range (-23.1) - (-17.9) kcal/mol, the contribution of electrostatic interaction energy varies in the range (-4.5) - (1.0) kcal/mol, and the torsional interaction energy varies in the range (2.5) - (4.6) kcal/mol. As can be seen from Table 6, the sequence of low-energy structures is almost the same as in the natural molecule. The first four low-energy conformations are the same as in the natural molecule. The relative energy of the B₃R B₁B₃B₃₂ conformation of the efee shape in the [Phe3]-rubiscolin molecule is 1.0 kcal/mol. This

conformation is the global conformation of the natural molecule. The contribution of electrostatic interaction energy to the stabilization of the conformation is the largest. In the conformation, the Pro2 amino acid residue, being in the R form of the main chain, rotates the following Phe3-Asp4-Leu5 tripeptide fragment in such a way that the positively charged N-side of the molecule and the negatively charged side chain of aspartic acid approach each other in space, and an effective interaction occurs between them, contributing up to (-12.2) kcal/mol to the total energy. In addition, the interaction energy between Pro2-Phe3 of Tpr1 contributes up to (-7.2) kcal/mol to the total energy, Pro2-Phe3 to (-2.2) kcal/mol, and Phe3-Asp4-Leu5 to (3.3) kcal/mol to the total energy (table 7). A comparison of tables 6, 7, and 8 with tables 1 and 2 shows that the values of the interaction forces stabilizing the molecules and the geometric parameters of the conformations are the same in both molecules.

The relative energy of the B₂R R₁R₁R₂₁ conformation of the efff shape in the [Phe3]-analog is 0 kcal/mol, while in the natural rubiscolin-5 molecule it is 0.4 kcal/mol. The interaction of Tyr-1 with the subsequent Pro2-Phe3-Asp4-Leu5 tetrapeptide fragment contributes to the stabilization of the conformation by (-17.8) kcal/mol, the interaction of Pro2 with the subsequent tripeptide fragment contributes to the total energy by (-5.1) kcal/mol, and the interaction of Phe3 with the subsequent dipeptide fragment contributes to the total energy by (-3.7) kcal/mol. Again, a comparison of Table 1 with Table 6, and Table 2 with Table 8 shows that the interaction forces and the values of the dihedral rotation angles of the molecules stabilizing this conformation in the natural rubiscolin-5 molecule and its [Phe3] analog are almost the same.

Another low-energy structure of the [Phe3]-rubiscolin molecule is the B₃R B₃B₃R₂₁ conformation belonging to the efef shape, whose relative energy in the native molecule was 0.2 kcal/mol. The non-valent interaction energy contributed up to (-20.7) kcal/mol to the stabilization of the conformation, the electrostatic interaction energy contributed up to (-3.7) kcal/mol, and the torsional interaction energy contributed up to (3.6) kcal/mol. In this conformation, the positively charged N-side of the molecule and the negatively charged side chain of Asp4 are spatially close to each other, contributing up to (-11.8) kcal/mol to the total energy, and a hydrogen bond is formed between the hydrogen atom of the main chain and the oxygen atom of the aspartic acid side chain. The Tyr1 amino acid residue and Pro2-Phe3 form an effective interaction, contributing (-5.9) kcal/mol to the total energy, while the Pro2 amino acid residue Phe3-Asp4 dipeptide fragment contributes (-3.0) kcal/mol to the total energy. Again, a comparison of Table 1 and Table 6, and Table 3 with Table 8, shows that the energy and geometric parameters of the analog and the native molecule are almost completely consistent.

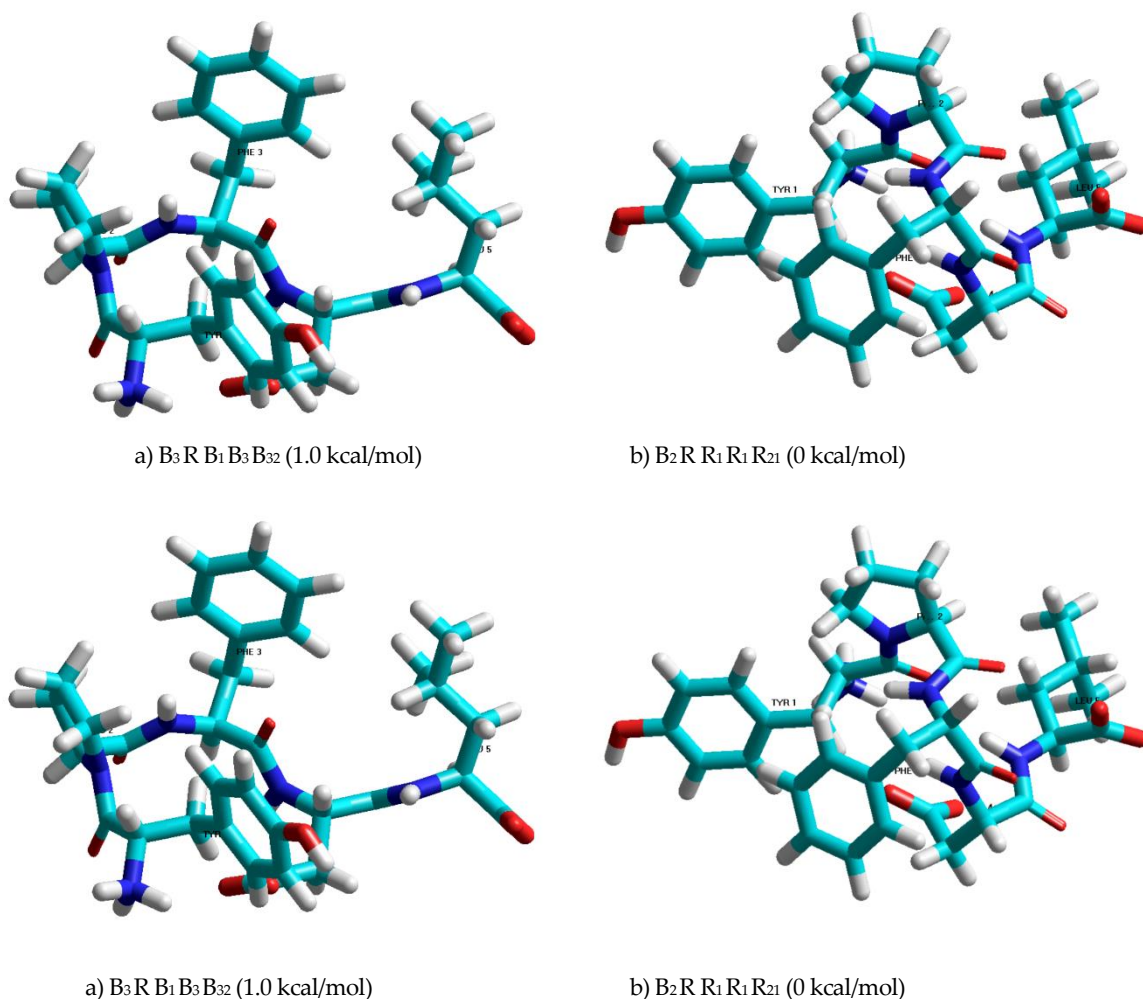


Figure 2. Atomic model of spatial structure of the [Phe3]- rubiscolin-5 molecule a), b), c) and d) corresponded to the structures with the relative energies 1.0 kcal/mol, 0 kcal/mol, 0 kcal/mol and 2.2 kcal/mol, respectively.

The relative energy of the $B_2 B_3 R_1 R_21$ conformation of the eeef shape is (2.2) kcal/mol. In the natural molecule, its relative energy was (4.0) kcal/mol. A comparison of the values of the energy and geometric parameters of these conformations in the corresponding tables shows that they agree very well.

The next four low-energy conformations of the [Phe3]-rubiscolin5 molecule, presented in Table 6, are similar to the conformations of the natural rubiscolin-5 molecule, shown in Table 1. The total contribution of the various interaction energies in all of the conformations, the interaction energies between the various amino acid residues, and the values of their dihedral rotation angles agree very well in the [Phe3]-rubiscolin-5 analog and the natural rubiscolin molecule.

Calculation of the spatial structure of the [Phe3]-rubiscolin-5 molecule showed that the values of its energy and geometric parameters given in Tables 6, 7, and 8, and the spatial arrangement of atoms in Figure 2 a,b,c,d, correspond to the values and figures given for the natural rubiscolin-5 molecule in the article [18]. Therefore, it can be concluded that the [Phe3] analog is also not a suitable analog for synthesis, and in principle it will retain all the functions of the natural molecule.

Conclusion

1. The spatial structure of the [Ile3]-rubiscolin-5 molecule was studied and it was shown that it is represented by eight low-energy conformations.
2. The roles of different interaction energies and interactions between different amino acid residues in the formation of low-energy conformations of the [Ile3]-rubiscolin-5 molecule were shown.
3. The low-energy conformations of the natural rubiscolin molecule and its [Ile3] analog were compared and it was shown that the energy and geometric parameters of both molecules were the same, and it was shown that the [Ile3]-analog was not a suitable analog for synthesis.
4. The three-dimensional spatial structure of the [Phe3]-rubiscolin analog was studied by the method of theoretical conformational analysis, the assembly of its low-energy conformations, the roles of various types of interactions in stabilizing them, and the values of dihedral rotation angles in low-energy conformations were determined.
5. Comparison of the energy and geometric parameters of the [Phe3]-rubiscolin-5 analogue and the natural rubiscolin-5 molecules showed that they are completely identical. Therefore, it cannot be assumed that this analogue will differ from the functions performed by the natural rubiscolin-5 molecule, and it is not advisable to synthesize the [Phe3]-analogue.

REFERENCES

1. Chesnokova E.A., Sarycheva N.Y., Dubynin V.A., Kamensky A.A. Food-Derived Opioid Peptides and Their Neurological Impact. *Advances in Physiological Sciences*, Vol.46, №1, p.22-46, 2015 (In Russ.).
2. Andersson I., Backlund A. Structure and function of Rubisco // *Plant Physiol. and Biochem.* 2008. V. 46. P. 275–291.
3. Wadley G., Martin A. The origins of agriculture: a biological perspective and a new hypothesis // *Austral. Biologist.* 1993. V. 6. № 96. P. 105–176. Wakefield A. J., Puleston J.M., Montgomery Yang S., Sonoda S., Chen L., Yoshikawa M.
4. Structure-activity relationship of rubiscolins as delta opioid peptides // *Peptides.* 2003. V. 24. № 4. 503–508.
5. Yang S., Yunden J., Sonoda S. et al. Rubiscolin, a delta selective opioid peptide derived from plant Rubisco // *FEBS Lett.* 2001. V. 509. № 2. P. 213–217.
6. Ohinata K., Agui S., Yoshikawa M. Soymorphins, novel mu opioid peptides derived from soy beta-conglycinin beta-subunit, have anxiolytic activities // *Biosci. Biotechnol. Biochem.* 2007. V. 71. № 10. P. 2618–2621.
6. Akhmedov N.A. Theoretical conformation analysis of β -casomorphin, valmuceptin and morphiceptin molecules. *Molecular. Biol.*, Vol.23, p.240-240,1989 (In Russ.).
7. Akhmedov N.A., Godjaev N.M., Suleymanova E.V., Popov E.M. Structural organization of the [Met]-enkephalin and endorphins molecules, Vol.16, p. 649-667,1990 (In Russ.).
8. Akhmedov N.A., Agayeva L.N., Ismailova L.I., Godjaev N.M. The spatial structure of the cardio active peptides. *Current Topics in Peptide and Protein Research*, Vol.11, p. 87-93, 2010.
9. Gadjeva Sh.N., Akhmedov N.A., Masimov E.A., Godjaev N.M. Spatial Structure of Thr-Pro-Ala-Glu-Asp-Phe-Met-Arg-Phe-NH₂. *Biophysics*, Vol.58, p.587-590, 2013 (In Russ.).
10. Akhmedov N.A., Ismailova L.I., Abbasli R.M. et al. Spatial Structure of Octarphin molecule. *IOSR J. Applied Physics (IOSR-JAP)*. Vol.8, p.66-70,2016.
11. Akhmedov N.A., Abbasli R.M., Agayeva L.N., Ismailova L.I. Three-dimensional structure of exorpin B5 molecule. *Conference proceedings Modern Trends In Physics*. p.201-104,2019.
12. Akhmedov N.A., Agayeva L.N., Akverdieva G.A., Abbasli R.M., Ismailova L.I. Spatial structure of the ACTH-(6-9)-PGP molecule. *J.Chem.Soc.Pak.*, Vol. 43. №5, p.500-504, 2021.
13. Agayeva L.N., Abdinova A.A., Akhmedova S.R., Akhmedov N.A. Spatial Structure of the ACTH-(7-10) Molecule. *Biophysics*, Vol.66, No4, p.531-534,2021.

14. Agaeva L.N, Abdinova A.A., Akhmedova S.R., Akhmedov N.F., and Akhmedov N.A. Spatial structure of Soymorphin-6 Molecule. *Biophysics*, Vol.68, № 6, p.1122-1127, 2023.
15. Ismailova L.I., Akverdieva G.A., Demukhamedova S.D., Akhmedov N.A. Molecular modelling of Pro-Gly gliproline and its complexes. *Moscow University Physics Bulletin*. Vol. 78, № 5, p. 668-680, 2023.
16. IUPAC-IUB. *Quantities, Units and Symbols in Physical Chemistry*, Blackwell Scientific, Oxford, 1993.
17. Maksumov I.S., Ismailova L.I., Godjaev N.M. Program for semi-empirical calculation of conformations of molecular complexes on a computer. *J.Struk.Chemistry*, Vol. 24, p.147-148, 1983.
18. Akhmedov N., Agayeva L., Abbasli R., Ismailova L. Spatial structure of rubiscolin-5 molecule. *Annali d'Italia* №30, p.5-8, 2022
19. Marta Sobolczyk, Renata Perlikowska. Rubiskoliny – biologiczne aktywne peptydy pochodzenia roślinnego. *Postepy Hig Med Dosw* (online), 2020; 74: 94–102.

UOT: 539.2/6:539/.04

DOI: <https://doi.org/10.30546/09081.2024.102.7065>

IMPACT OF SULFUR ION CONCENTRATION ON THE OPTICAL AND STRUCTURAL CHARACTERISTICS OF Ag-Ag₂S Core-Shell NANOSTRUCTURES

Fatma ISMAYILOVA*, Mustafa MURADOV, Mahammad Baghir BAGHIROV,
Goncha EYVAZOVA, Sevinj MAMMADYAROVA

Nano Research Laboratory,
Baku State University, Z. Khalilov st.23, AZ-1148,
Baku, Azerbaijan

ARTICLE INFO	ABSTRACT
<p>Article history: Received: 2024-11-30 Received in revised form: 2025-01-08 Accepted: 2025-02-10 Available online</p> <p>Keywords: Core-shell structures, Surface Plasmon Resonance, Ionic diffusion</p>	<p><i>In this study, silver nanoparticles (AgNPs) were synthesized via chemical reduction. Then Ag-Ag₂S core-shell structures were synthesized by simply mixing different concentrations of Na₂S aqueous solution (5,10 and 15mM) and AgNPs. The structural and optical properties of these structures were analyzed. Changes in the structure of the samples were analyzed by X-ray diffraction (XRD). The optical properties and bandgap values were studied using ultraviolet-visible (UV-Vis) spectroscopy. The structural and optical properties of AgNPs revealed clear differences in their physical properties after sulfidation. From the study of optical properties, we determined that Ag-Ag₂S core-shell structures have broadband absorption properties that can be controlled by changing the concentration of sulfur ions in the sulfidation process. Also, because of sulfidation, it was determined that the value of the bandgap of Ag-Ag₂S structures changes.</i></p>

1. Introduction

In recent years, much attention has been paid to the controlled synthesis of silver-based nanostructures because the catalytic, electronic, and optical properties of these materials can be tuned by changing their composition, shape, size, and structure [1–6]. Among the noble metals, Ag is a promising material for industrial applications because of its non-toxicity and relatively low cost compared to other noble metals. In addition, Ag nanoparticles have a unique localized surface plasmon resonance (SPR) effect that enables light absorption in the visible region of the solar spectrum, thereby enhancing photocatalytic performance [7]. At the same time, Ag nanomaterials are actively used in catalysis, medicine, microelectronics, and other fields due to their surface effect, quantum size effect and high electrical conductivity [8, 9]. As is well known, Ag₂S is a semiconductor with unique physical properties. Ag₂S has low toxicity, non-linear optical properties and exhibits high chemical stability [10-12]. Noble metal-semiconductor hybrid nanostructures are increasingly being explored for their multifunctional capabilities and improved physical and chemical properties compared to their constituents [13, 14]. Among them, Ag-Ag₂S hybrid nanostructures are of practical interest due to their tunable plasmon properties [15]. These optical properties directly depend on the morphology and composition of

the Ag-Ag₂S hybrid nanostructures. Ag-Ag₂S hybrid nanostructures, in particular, exhibit enhanced chemical and thermal stability, tunable plasmonic properties, and exceptional photocatalytic activity. These properties result from synergistic effects between metallic silver and semiconducting silver sulfide components within the nanostructure. These properties of Ag-Ag₂S nanostructures create their highly promising materials for application. These fields can be used in photonic devices, sensor technologies, and biomedical applications [16,17]. At the same time, Ag-Ag₂S nanostructures can be applied as photocatalysts with high efficiency, which allows them to be used in processes such as water splitting and neutralization of natural pollutants [18]. In addition, the wide bandgap of Ag-Ag₂S nanostructures makes them suitable materials for high-quality optical imaging and infrared (IR) detectors. In particular, the use of these materials in applications such as infrared photodetectors and solar cells has become the subject of extensive research [19-21]. Studies on Ag₂S have shown that compared with conventional metal oxide semiconductors, metal sulfides have narrow band gaps and are more efficient in the use of sunlight [22]. Regardless of their morphology, particle size, and coating materials, Ag nanoparticles easily react with sulfides to form silver sulfide (Ag₂S), resulting in Ag-Ag₂S structure and high photocatalytic properties [23].

In this study, the successful synthesis of Ag-Ag₂S core-shell nanostructures was achieved. When Na₂S solution with different concentrations was added to the dispersion of Ag nanoparticles at room temperature, a sulfidation reaction occurred on the surface of Ag nanoparticles and core-shell Ag-Ag₂S structures were formed. The degree of sulfidation of AgNPs can be controlled by changing the concentration of sulfur ions added to the dispersion of AgNPs, which allows the morphological control of Ag-Ag₂S nanostructures. The structural and optical properties of AgNPs and Ag-Ag₂S structures were studied in detail.

2. Materials and methods

2.1 Synthesis of silver nanoparticles and preparation of Ag-Ag₂S core-shell structures

The studied work involved the synthesis of Ag nanoparticles via the chemical reduction method [24,25]. Silver nanoparticles were prepared by reducing silver nitrate using a PVA aqueous solution as a coating agent. A silver nitrate solution was prepared by adding 0.03 g of silver nitrate (AgNO₃) to 10 ml of distilled water. Sodium borohydride (NaBH₄) was dissolved in 20 ml of distilled water and added to the PVA solution. The prepared PVA solution was heated to 60°C and stirred. Then AgNO₃ solution was added dropwise to the PVA solution. The color of the mixture began to darken with the dropwise addition of AgNO₃ solution. After all silver nitrate (AgNO₃) solution was added, the mixed solution was stirred in a magnetic stirrer for another 10 min.

Sodium sulfide (Na₂S) was used as a source of sulfur adsorbed on the surface of the synthesized silver nanoparticles. The synthesized Ag-Ag₂S structures were chemically synthesized by changing the concentration of sulfur ions from 5 to 15mM in the Na₂S solution, whereas the concentration of AgNPs remained unchanged. Then, the prepared aqueous solution of sulfur ions was added dropwise to the AgNP solution under continuous stirring. The resultant solution was kept under magnetic stirring for 4 hours and color change of the suspension indicated the formation of Ag-Ag₂S structures. It was washed several times using DI water and the suspension was used for various characterization.

2.2 Analysis methods

The structural investigation was performed utilizing a Rigaku Mini Flex 600 X-ray diffractometer ($k = 1/4$ 1.54060 Å) using Ni-filtered Cu K_{α} radiation. Optical properties were examined using the UV-VIS Specord 250 Plus spectrophotometer.

3. Results and discussion

3.1 X-ray diffraction analysis

To determine crystal structure of synthesized AgNPs and Ag-Ag₂S hybrid nanostructures were analyzed by XRD and diffractograms are shown in Figure 1. In Figure 1a, peaks corresponding to (111) and (220) planes observed at $2\theta = 38.33^{\circ}$ and 64.63° are characteristic of face-centered cubic crystal structure of AgNPs which revealed JCPDS No. 04-0783 card number [26]. In this pattern observation of broad diffraction peaks indicates that the particle size is small. Figure 1b shows the XRD pattern of Ag-Ag₂S nanostructures synthesized using with 5mM concentration of Na₂S. As can be seen from the pattern, a new peak at $2\theta = 32.6^{\circ}$ is observed corresponding to (112) index. This peak is characteristic of Ag₂S formed on the surface of AgNPs which is characteristic for monoclinic phase of Ag₂S and correspond to (112) Miller index and JCPDS No. 14-0072 card number [27]. In the diffraction pattern, by the increasing of the concentration of sulfur ions, the peaks of Ag₂S peaks also increases. This result is due to the increase in the concentration of sulfur ions in the Na₂S solution, which causes AgNPs to be exposed to the more Na₂S solution and more sulfur ions penetrate the nanoparticles. As can be seen from the spectrum in Figure 1b, new peaks for Ag₂S corresponding to the (012), (-112), (-121) and (-103) planes observed at 22.3° , 30.12° , 34.35° , and 37.8° , respectively which correspond to monoclinic phase of Ag₂S. This result is in good agreement with JCPDS No. 14-0072 standard data [28]. This confirms the crystallization of Ag-Ag₂S structures. Thus, an increase in the concentration of Na₂S increases the amount of Ag₂S formed on the surface of the nanoparticles. In addition, although the intensity of the main peak for AgNPs decreased compared with the original sample, the characteristic peaks of AgNPs did not disappear in all spectra, which indicates that not all AgNPs in the sample were converted to Ag₂S and are formed as Ag-Ag₂S heterostructures. The obtained peaks were in good agreement with the characteristic peaks and confirmed the formation of AgNPs and Ag-Ag₂S structures.

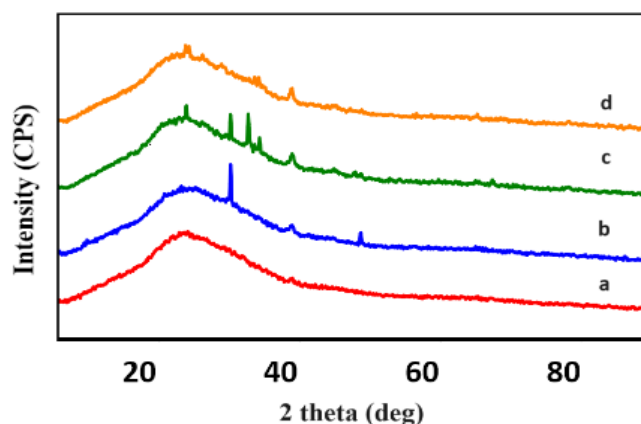


Fig.1 XRD patterns of (a) AgNPs, (b) Ag-Ag₂S (5mM), (c) Ag-Ag₂S (10mM), (d) Ag-Ag₂S (15mM)

3.2 UV-Vis spectroscopy

Figure 2A shows the optical absorption spectrum of silver nanoparticles (AgNPs) and Ag-Ag₂S structures with different concentrations. The absorption spectrum shows a characteristic peak at 385 nm. This is consistent with the surface plasmon resonance of AgNPs [29]. This spectrum demonstrates that AgNPs were successfully synthesized. An aqueous solution of Na₂S was added to the dispersion of Ag nanoparticles in different amounts. The sulfidation reaction was monitored by recording the absorption spectra of the reaction solution and altering the Na₂S concentration. However, a decrease in optical absorption was observed after sulfur (S) doping at low concentrations of Na₂S. This decrease is related to AgNP sulfidation and changes in nanoparticle surface properties. When the samples are exposed to the Na₂S solution, the intensity of the peak associated with Ag nanoparticle surface plasmons decreases. Along with the decrease in intensity, a red shift is observed at low and medium concentrations of sulfur ions. This result is due to the effect of Na₂S on the surface of Ag nanoparticles and the reduction of the plasmon oscillations characteristic of Ag nanoparticles. In addition, after the concentration of sulfur ions reached 10 mM, the red shift of the peaks became sharper and an increase in the wavelength of the plasmon peaks of the samples was observed (Figure 2A). The frequency of plasmon peaks depends on the concentration of free electrons (equation 1) [30]. It is known that a redshift in the wavelength causes decreasing of the frequency. This is due to a decrease in the electron concentration. At the same time, the experimentally observed redshift during the sulfidation process can be attributed to the differences in the sulfidation rate on different sides of the silver nanoparticles [31]. Based on the experimental results, we can conclude that the reduction in the size of the Ag nanoparticle (i.e., the replacement of several atomic layers of the silver nanoparticle with Ag₂S layers) is the most likely explanation for the redshift of AgNPs observed during sulfidation. There are two main reasons why Ag-Ag₂S core-shell structures have broadband absorption properties: First, the red shift of the absorption spectra is associated with the formation of the Ag₂S dielectric layer, which is in good agreement with the literature [33,34]. The reason is that the LSPR (Localized Surface Plasmon Resonance) of Ag nanostructures is sensitive to changes in the surrounding dielectric medium [35]. On the other hand, the broadband absorption of Ag-Ag₂S core-shell structures is related to the gradually changing Ag₂S shell thickness. Using of Na₂S solution, an Ag₂S semiconductor layer is formed on the metallic AgNPs, which is associated with a decrease in electron concentration compared with the first sample.

$$\omega = \sqrt{\frac{ne^2}{\epsilon_0 m^*}} \quad (1)$$

ω is the plasmon resonance frequency, n is the concentration of free electrons, e is the elementary charge, ϵ_0 is the vacuum permeability, and m^* is the effective mass of the electron. According to Equation 1, the calculated concentrations of electrons on the surface of the Ag-Ag₂S structure at different concentrations of Na₂S are given in Table 1. The following is the formation mechanism of Ag-Ag₂S core-shell type structures: sulfidation starts from defects on the surface of Ag nanoparticles [36] and Ag₂S is formed. Sulfur ions undergo two types of diffusion when a small amount of Ag₂S islands are formed on the surface of Ag nanoparticles. It spreads until it reaches its already-formed islands. In the second type of diffusion, with an increase in the concentration of sulfur ions, the amount of Ag₂S on the surface and in the volume relative to Ag increases at different rates. It is clear that surface diffusion is faster than volume diffusion. After penetrating the Ag₂S layers formed by increasing concentrations of sulfur ions, the amount of light reaching

the main surface of Ag decreases, which causes unstable excitation of the plasmon on the Ag surface. At the highest concentration of sulfur ions, the thickness of the surface layers begins to increase. Since the thickness of the volume layer is controlled by diffusion, its thickness does not change. Instead, it further reduced the size of the Ag core.

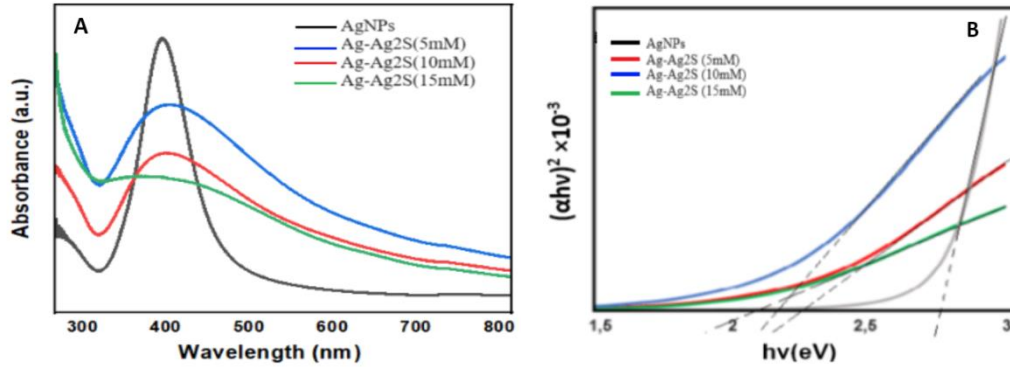


Fig.2 UV-Vis absorption spectra (A) and width of the forbidden band (B) of samples with Ag nanoparticles and Na₂S solution.

Table.1 Plasmonic parameters of Ag-Ag₂S structures prepared at different concentrations.

Nanostructure	Experimental plasmon peaks (nm)	Concentration of plasmon electrons	Band gap
Ag-Ag ₂ S (5mM)	395	$6.92 \times 10^{24} \text{ cm}^{-3}$	2.25 eV
Ag-Ag ₂ S (10mM)	399	$6.77 \times 10^{24} \text{ cm}^{-3}$	2.19 eV
Ag-Ag ₂ S (15mM)	403	$6.15 \times 10^{24} \text{ cm}^{-3}$	2.10 eV

The band gap values of the samples were determined using the Tauc method.

$$(ahv)^2 = A(hv - E_g) \quad (2)$$

$h\nu$ is the photon energy, A is a constant that depends on the structure and type of the sample, E_g is the band gap, and the value of n depends on the nature of the transition: $n = 2$ for direct allowed transition, $n=1/2$ for indirect allowed transition, α is the absorption coefficient, its value is obtained from the Beer-Lambert formula. As shown in Figure 2B, the pure AgNPs have a band gap of 2.8 eV. This value is related to the optical properties of Ag and quantum size effects. Also, as seen in Figure 2B, the bandgap at different concentrations of Na₂S solution obtained different values: 2.25 eV at 5 mM concentration, 2.19 eV at 10 mM concentration, and 2.10 eV at 15 mM concentration. When Ag nanoparticles react with Na₂S solution, Ag₂S is formed on their surface. The kinetics of this reaction depend on the solution concentration. At higher concentrations, the reaction was faster, resulting in more Ag₂S being formed. The thickness of the Ag₂S layer formed on the surface of Ag particles during the reaction increased with increasing concentration. In 5 mM Na₂S solution, the surface of Ag particles was covered with a small amount of Ag₂S, as a result, the band gap decreased to 2.25 eV. In 10 mM and 15 mM Na₂S solutions, the Ag₂S layer is thicker, and as a result, the bandgap decreases from 2.19 eV to 2.10 eV, respectively. The formation of Ag₂S narrows the band gap of Ag nanoparticles because the Ag₂S material has a different electronic structure than pure Ag. As the Ag₂S layer on the surface thickens, the quantum size effect of the Ag nanoparticle weakens and the band gap decreases. According to the available literature, the bandgap of Ag₂S nanocrystals is in the range of $E_g = 0.9-1.1$ eV [37]. Consequently, the analysis of the results shows that the introduction of sulfur (S) can

lead to changes in the bandgap of Ag-Ag₂S core-shell type structures. The reason for this is that the excited electrons passing into the conduction band of Ag₂S easily transfer to silver at the Ag-Ag₂S interface. The formation of Ag and Ag₂S heterostructure changes the structure of the band gap of Ag₂S at the interface, facilitates the separation of charges, and reduces the recombination of charge carriers.

4. Conclusion

In this study, silver nanoparticles were synthesized via chemical reduction. Then, Ag-Ag₂S core-shell structures were prepared by adding different concentrations of Na₂S solution to AgNPs. The properties of AgNPs and Ag-Ag₂S structures were studied. The structural analysis results showed that a layer of Ag₂S formed on the surface of the AgNPs because of the sulfidation process. In addition, there was a decrease in the degree of crystallization of AgNPs. This structural change depends on the increase in the concentration of sulfur ions. Moreover, UV-Vis spectroscopy showed that the intensity of the plasmon oscillation peaks of the silver nanoparticles decreased and a red shift occurred with increasing concentrations. In addition, the band gap decreased from 2.25 eV to 2.10 eV. It can be associated with the formation of Ag₂S nanoparticles.

REFERENCES

1. B.S.Hoener et al. Plasmonic sensing and control of single-nanoparticle electrochemistry, *Chem* 4 (2018) 1560-1585.
2. S.Rostami, A.Mehdinia, A.Jabbari. Seed-mediated grown silver nanoparticles as a colorimetric sensor for detection of ascorbic acid, *Spectrochimica Acta Part A Molecular and Biomolecular Spectroscopy*, 180 (2017) 204-210.
3. M.Chen, Y.He, J.Zhu. Preparation of Au-Ag bimetallic nanoparticles for enhanced solar photothermal conversion, *International Journal of Heat and Mass Transfer*, 114 (2017) 1098- 1104.
4. A.Decharat, S.Wagle, S.Jacobsen, F.Melandso. Using Silver Nano-Particle Ink in Electrode Fabrication of High Frequency Copolymer Ultrasonic Transducers: Modeling and Experimental Investigation. *Sensors*, 15 (2015) 9210-9227.
5. Q.Huang, W.Shen, Q.Xu, R.Tan, W.Song. Properties of polyacrylic acid-coated silver nanoparticle ink for inkjet printing conductive tracks on paper with high conductivity. *Mater. Chem. Phys*, 147 (2014) 550-556.
6. A.Hu, J.Y.Guo, H.Alarifi, G.Patane, Y.Zhou, G.Compagnini, C.X.Xu. Low temperature sintering of Ag nanoparticles for flexible electronics packaging. *Appl. Phys. Lett*, 97 (2010) 153117.
7. J.Low et al. Direct evidence and enhancement of surface plasmon resonance effect on Ag-loaded TiO₂ nanotube arrays for photocatalytic CO₂ reduction. *Applied Surface Science*, 434 (2018) 423-432.
8. P.Panchal, D.R.Paul, A.Sharma, P.Choudhary, P.Meena, S.P.Nehra. Biogenic mediated Ag/ZnO nanocomposites for photocatalytic and antibacterial activities towards disinfection of water, *J.Colloid Sci*, 563 (2020) 370-380.
9. X.Liu, J.Iocozzia, Y.Wang, X.Cui, Y.Chen, S.Zhao, Z.Lee, Z.Lin. Noble metal-metal oxide nanohybrids with tailored nanostructures for efficient solar energy conversion, photocatalysis and environmental remediation. *Energy Environ. Sci*, 10 (2017) 402-434.
10. J.Feng, X.Li, Z.Shi, C.Zheng, X.Li, D.Leng, Y.Wang, J.Liu, L.Zhu. *Adv. Opt. Mater*, 8 (2020) 1901762.
11. C.Ding, Y.Huang, Z.Shen, X.Chen. *Adv. Mater*, 33 (2021) 2007768.
12. A.Badawi, S.S.Alharthi. *Mater. Sci. Semicond. Process*, 116 (2020) 105139.
13. N.Zhang et al. Function-oriented engineering of metal-based nanohybrids for photoredox catalysis: exerting plasmonic effect and beyond, *Chem*, 4.8 (2018) 1832-1861.
14. S.I.Sadovnikov et al. Enhanced photocatalytic hydrogen evolution from aqueous solutions on Ag₂S/Ag heteronanostructure, *International Journal of Hydrogen Energy*, 42 (2017) 25258-25266.
15. J.Zhao, Hundred, J.Xing, Y.Zou, H.Liu, H.Zhang, W.Yu, H.Idriss, C.Guo. Effect of Ag₂S Nanocrystals/Reduced Graphene Oxide Interface on Hydrogen Evolution Reaction. *Catalysts*, 10 (2020) 948.

16. J.Xiong, C.Han, W.Li, Q.Sun, J.Chen, S.Chou, Z.Li, S.Dou. Ambient synthesis of a multifunctional 1D/2D hierarchical Ag-Ag₂S nanowire/nanosheet heterostructure with diverse applications. *CrystEngComm*, 18 (2016) 930-937.
17. M.M.Shahjamali, Y.Zhou, N.Zaraee, C.Xue, J.Wu, N.Large, C.A.Mirkin. Ag-Ag₂S hybrid nanoprisms: structural versus plasmonic evolution, *Acs Nano*, 10 (2016) 5362-5373.
18. B.Díez-Buitrago et al. Facile synthesis and characterization of Ag/Ag₂S nanoparticles enzymatically grown in situ and their application to the colorimetric detection of glucose oxidase, *ChemistrySelect*, 4,28 (2019) 8212-8219.
19. A.Pradyasti et al. Ag-Ag₂S hybrid nanoplates with unique heterostructures: Facile synthesis and photocatalytic application, *Journal of Alloys and Compounds*, 826 (2020) 154191.
20. X.H.Wang, B.Shi, Y.Fang, F.Rong, F.F.Huang, R.H.Que, M.W.Shao. High capacitance and rate capability of a NiS₂@CdS core-shell nanostructure supercapacitor, *J. Mater. Chem. A*, 5 (2017) 7165-7172.
21. R.Marin et al. Nanoprobes for Biomedical Imaging with Tunable Near-Infrared Optical Properties Obtained via Green Synthesis, *Advanced Photonics Research*, 3,1 (2022) 2100260.
22. D.Ruiz et al. Ag/Ag₂S nanocrystals for high sensitivity near-infrared luminescence nanothermometry, *Advanced Functional Materials*, 27,6 (2017) 1604629.
23. B.M.Al-Shehri, M.Shkir, T.M.Bawazeer, S.AlFaify, M.S.Hamdy. *Phys. E*, 121 (2020) 114060.
24. S.H.Lee, B.H.Jun. Silver Nanoparticles: Synthesis and Application for Nanomedicine, *Int. J. Mol.Sci*, 20 (2019) 865.
25. A.Syafiuddin, Salmiati, M.R.Salim, A.B.H.Kueh, T.Hadibarata, H.A.Nur. Review of silver nanoparticles: Research trends, global consumption, synthesis, properties, and future challenges. *J. Clin. Chem. Soc*, 64 (2017) 732-756.
26. J.Lu, D.Liu, J.Dai. *J. Mater. Sci.: Mater. Electron*, 30 (2019) 15786-15794.
27. K.Sahraoui, N.Benramdane, M.Khadraoui, R.Miloua, C.Mathieu. Characterization of silver sulphide thin films prepared by spray pyrolysis using a new precursor silver chloride, *Sensors & Transducers*, 27 (2014) 319-325.
28. A.Gusev, S.J.Sadovnikov. Acanthite-argentite transformation in nanocrystalline silver sulfide and the Ag₂S/Ag nanoheterostructure, *Semiconductors*, 50 (2016) 682-687.
29. K.Khurana, N.Jaggi. Localized surface plasmonic properties of Au and Ag nanoparticles for sensors: A review, *Plasmonics*, 16,4 (2021) 981-999.
30. M.B.Gebeyehu, T.F.Chala, S.Y.Chang, C.M.Wu, J.Y.Lee. *RSC Adv*, 7 (26) (2017) 16139-16148.
31. M.M.Shahjamali et al. Ag-Ag₂S hybrid nanoprisms: structural versus plasmonic evolution, *Acs Nano*, 10,5 (2016) 5362-5373.
32. J.Xiong et al. Ambient synthesis of a multifunctional 1D/2D hierarchical Ag-Ag₂S nanowire/nanosheet heterostructure with diverse applications, *CrystEngComm*, 18 (2016) 930-937.
33. J.Zeng, J.Tao, D.Su, Y.Zhu, D.Qin. Selective sulfuration at the corner sites of a silver nanocrystal and its use in stabilization of the shape, *Nano Lett*, 11 (2011) 3010-3015.
34. M.Pang, J.Hu, H.C.Zeng. Synthesis, morphological control, and antibacterial properties of hollow/solid Ag₂S/Ag heterodimers, *Journal of the American Chemical Society*, 132,31 (2010) 10771-10785.
35. G.Park, C.Lee, D.Seo, H.Song. Full-Color Tuning of Surface Plasmon Resonance by Compositional Variation of Au@Ag Core-Shell Nanocubes with Sulfides, *Langmuir*, 28 (2012) 9003-9009.
36. R.Zamiri, H.A.Abbastabar, A.Zakaria, G.Zamiri, M.Shabani, B.Singh, J.M.F.Ferreira. *Chem.cent. J*, 9 (2015) 1-6.
37. A.Nekooei, M.R.Miroliaei, M.S.Nejad, & H.Sheibani, Enhanced visible-light photocatalytic activity of ZnS/S-graphene quantum dots reinforced with Ag₂S nanoparticles. *Materials Science and Engineering: B*, 284, (2022). 115884.

UOT:539.219.3:358.931-405

DOI: <https://doi.org/10.30546/09081.2024.102.7068>

GALVANOMAGNETIC PROPERTIES OF $Gd_xSn_{1-x}Se$ SOLID SOLUTIONS

O.M.HASANOV¹, C.I.HUSEYNOV¹, H.A.ASLANOV¹, X.A.ADGOZALOVA¹,
G.A.GARASHOVA¹, R.B.BAYRAMLI²

¹Azerbaijan State Pedagogical University

AZ-1000, Baku, Uz. Hajibeyli Str.68, Baku, Azerbaijan

cahangir.adpu@mail.ru

²Baku Engineering University

AZ0101, Khirdalan city, Hasan Aliyev str. 120, Absheron, Azerbaijan

rabayramov@beu.edu.az

ARTICLE INFO	ABSTRACT
<p>Article history: Received: 2024-12-18 Received in revised form: 2025-02-10 Accepted: 2025-02-10 Available online</p> <p>Keywords: solid solution, crystal parameters, specific electrical conductivity, Hall coefficient, magnetoresistance, zone structure</p>	<p>The nature of the interaction in the SnSe – GdSe quasibinary section was studied, the solubility region of GdSe in SnSe was determined, $Gd_xSn_{1-x}Se$ solid solutions were obtained, complex physicochemical analyses were carried out and crystal parameters of the sample were determined. The specific electrical conductivity, Hall coefficient, and magnetic resistance of $Gd_xSn_{1-x}Se$ solid solutions were studied in the temperature range of 300-650 K, and the charge transport mechanisms were investigated. The dependence of magnetic resistance on composition, temperature, and magnetic field intensity was studied. The chemical bond and crystallization type structure in Tin monoselenide has also been investigated. Using a special X-ray diffractometer, the X-ray structural analysis was carried.</p>

1. Introduction

Interest in semiconductor compounds of the A^4B^6 type is due to the prospects for their use in semiconductor instrumentation. For example, SnS and $SnSe$ are used as a base material for creating active elements that operate in the infrared region of the optical spectrum, in thermodynamic converters [1-2], an absorbing layer in thin-film solar energy converters [3-4], and also as photoconductors [5], semiconductor sensors [6], micro-batteries [7]. The fundamental characteristics of these compounds a small band gap, high permittivity, relatively high radiation resistance, and the predominance of ionic bonding - further expand the possibilities of their application [8]. In recent years, much effort has been directed at creating photovoltaic devices from cost-effective, low-toxic, low-cost materials with a simple production technology. In this regard, SnSe semiconductor compounds have proven to be very promising due to the low cost of the material, which is due to the widespread occurrence of tin and selenium in nature.

Tin monoselenide has a complex ionic-covalent chemical bond and crystallizes in the $NaCl$ –type structure. One of the main features of SnSe is the presence of defects to a certain extent [9]. It was found that the presence of vacancies in both sublattices and their interaction is

caused by antistructural $\sim 10^{17} \text{ cm}^{-3}$ defects. A high concentration of these defects in *SnSe* leads to the formation of p-type conductivity. Tin selenide is a base material for creating active elements that operate in the infrared region of the optical spectrum, as well as in thermodynamic converters [10,11].

Doping them with impurities that create quasi-local levels expands the possibilities of their practical application. The introduction of rare earth metal (REM) elements into tin monoselenide causes the emergence of a number of physical properties associated with the nature of the defect and the interaction of defects. The behavior of REM impurities in semiconductors is characterized by some distinctive features, for example, a combination of low solubility and the ability of REM to "purify" the material, which makes it possible to significantly reduce the concentration of background impurities and defects [12].

The corresponding studies are of particular importance in fundamental physics, as well as from the point of view of their application. Substances obtained with the participation of rare earth metals (REM) are widely used in the manufacture of some converters of electrical energy, various types of thermistors resistant to radiation, pressure and humidity. With incomplete filling of the electronic structure of REM level $4f$, an easy transition to $4f - 5d - 6s$ occurs, and the creation of a variable valence due to mobile electrons of atoms of level $4f$ makes the materials obtained with their participation an interesting object of study. From this point of view, the possibility of obtaining new promising materials with the required physical properties based on alloys and compounds with the participation of REM makes their study especially important [13, 14]. Therefore, the study of the interaction between chalcogenides *SnSe* and *GdSe*, as well as a comprehensive study of the galvanomagnetic properties of the formed solid solutions is of scientific and practical interest.

2. Experimental procedure

The initial components of tin macri "B4-000", selenium grade "OC417-4" and chemically pure prosedium (99.98%) were used to synthesize the *SnSe - GdSe* alloys. The synthesis was carried out in evacuated quartz ampoules, at a pressure of 0.1333 Pa, by the method of direct melting of the components in two stages. At the initial stage, the ampoule together with the substance was heated to the melting point of selenium at a rate of 4 – 5 degrees / minute and maintained at this temperature for 3 – 4 hours, then the temperature was gradually increased depending on the composition to 950 – 1000 °C, and maintained for 8 – 9 hours. The synthesized samples for complex physicochemical analysis and electrophysical studies were annealed for 140 – 210 hours depending on the composition: the annealing time was increased with an increase in the gadolinium content. Homogenizing annealing of the obtained single-phase samples was carried out in a spectrally pure argon environment.

The interaction in the *SnSe - GdSe* system was studied by differential thermal analysis (DTA), X-ray phase analysis (XPA), microstructural analysis (MSA), as well as by measuring microhardness and determining the density. To determine the thermal effects of the obtained samples and phase transitions, DTA was carried out on a Perkin Elmer Sinintltaneons Thermal Analgiyzer, STA 6000 (USA). Nitrogen was used as the working gas with a feed rate of 20 ml/sec, the sample is heated to melting at a heating rate of 5 °C/min.

X-ray structural analysis was carried out on a Miniflex X-ray diffractometer by Rigaku Corporation, operating at 30 kV, 10 mA, and $\text{CuK}\alpha$ radiation ($\lambda = 1.5406 \text{ \AA}$). Diffraction

reflections were observed at a displacement angle of 2θ in the range of $0-80^\circ$. A Japanese JEOL JSM6610-LV scanning electron microscope was used to study the morphology and microcomposition of the sample surface. The galvanomagnetic properties of samples of different compositions obtained in the field of solid solutions of the quasi-binary compound $(SnSe)_{1-x} - (GdSe)_x$ were studied in a wide temperature range, and an analysis of the general pattern was carried out. The specific electrical conductivity (σ), Hall coefficient (R), and relative magnetic resistance ($\Delta\rho/\rho$) were measured in the temperature range of $300 \div 650K$ in a constant magnetic field in the mode direct current [15]. The experimental error did not exceed 4.2%.

3. RESULTS AND DISCUSSION

3.1. Physicochemical analysis

Sharp peaks corresponding to melting and solidification are observed on the heating and cooling curves in the thermograms of the obtained $Gd_xSn_{1-x}Se$ alloy system. This allows us to state that congruently melting alloys are formed during the synthesis. In the binary compound $SnSe$, partial replacement of Sn atoms by Gd atoms contributes to a decrease in the melting temperature, which apparently causes REE in these crystals to act as softeners.

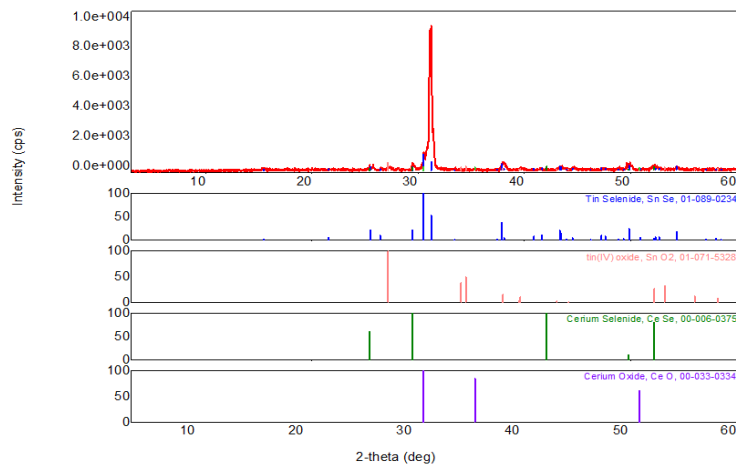


Fig. 1. X-ray diffraction spectrum of crystals $Gd_xSn_{1-x}Se$: 2- $x=0,005$

An analysis of the intensities of X -ray reflections shows the presence of a predominant direction in the crystal, and also that the studied sample consists of a single phase. Indexing of X -ray patterns shows that in the solubility region of Gd based on $SnSe$, the studied alloys crystallize in the orthorhombic syngony with the space group $D_{2h}^{16}-P_{cmn}$ (Fig. 1). In the X-ray diffraction patterns in the range $0 \leq x \leq 0.02$, no shifts of diffraction lines are observed, and only a change in their intensity in the specified range indicates that solid solutions based on $SnSe$ have formed. In the binary compound $SnSe$ in the dissolution region, due to the partial replacement of Sn atoms by rare-earth metal atoms of larger radius, the intensity of reflections decreases and the parameters of the orthorhombic unit cell of the lattice increase additively. In this region, the growth of the lattice parameters is linear and no deviation from Vegard's law is observed.

From the analysis of X -ray structural data it follows that with the introduction of gadolinium selenide an increase in the parameters of the unit cell of $SnSe$ is observed as the

concentration of *Gd* increases, as well as intense scattering of carriers by lattice "distortions" coinciding with studies of the thermal conductivity of alloys [16]. With an increase in the *Gd* content in the alloy, the density of $Gd_xSn_{1-x}Se$ does not change significantly. This confirms that the *Gd* atoms introduced by us into the $Gd_xSn_{1-x}Se$ alloy primarily occupy the interstitial vacant place in the crystal, i.e. defect formation occurs according to Frenkel [17].

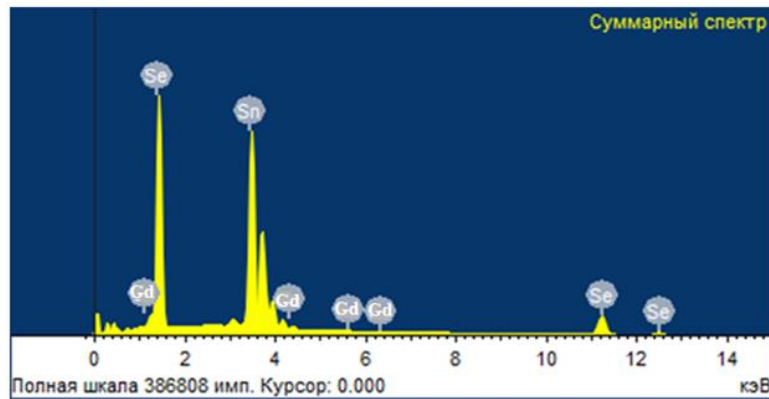


Fig. 2. X-ray microanalysis of the crystal surface $Gd_xSn_{1-x}Se$: 2- $x=0,005$

The observed growth of the lattice parameters, good agreement of partial substitution of *Sn* atoms by *Gd* atoms of larger radius and observance of Vegard's law allow us to speak about the formation of solid substitution solutions based on *SnSe*. A study of the dependence of the microstructure, microhardness and density of the composition, also revealed by X-ray and pycnometric methods, shows that the region of dissolution of *GdSe* in *SnSe* at room temperature is limited to 2 mol%.

The results of the conducted complex physicochemical analyses show that the $Gd_xSn_{1-x}Se$ alloy system, like the main substance *SnSe*, crystallizes in the orthorhombic syngony. With an increase in the percentage of *GdSe* in the composition, a weak increase in the parameters of the unit cell of the crystal lattice, density and microhardness is observed, and the thermal effects shift to the region of relatively lower temperatures.

Since the atoms of *Sn* and *Gd* belong to different subgroups, differ greatly in electron configurations, the sizes of the atoms of the soluble element differ from the sizes of the solvent atom, therefore, when a solid substitution solution of $Gd_xSn_{1-x}Se$ is formed, the *SnSe* crystal lattice is slightly distorted, without losing its basic structure.

Quantitative X-ray microanalysis determined the phase composition and distribution of chemical elements on the surface of the sample under study (Fig. 2). Analysis of the results obtained shows surface homogeneity, but with a change in stoichiometry within the homogeneity region of *SnSe* on the side of excess selenium.

3.2. Electrical conductivity in solid solutions $Gd_xSn_{1-x}Se$

With an increase in the amount of *Gd* in small concentrations in the $Gd_xSn_{1-x}Se$ alloy system, the specific electrical conductivity decreases, and at $x > 0.01$, an increase in electrical conductivity is observed. At *Gd* concentrations $0 \leq x \leq 0.01$, filling of tin vacancies and a change in chalcogen antistructural defects leads to a decrease in the values of the charge carrier concentration and specific electrical conductivity. It can be said that with a subsequent increase in the amount of *GdSe*, antistructural defects do not occur. It is very likely that a partial increase

in specific electrical conductivity is associated with the appearance of the second type of charge carriers as a result of the action of donor Gd atoms.

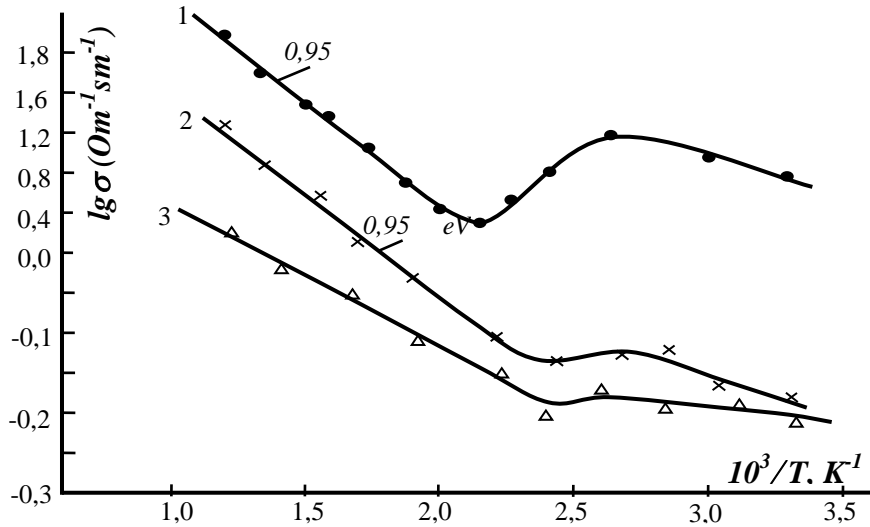


Fig. 3. Temperature dependence of electrical conductivity of solid solutions $Gd_xSn_{1-x}Se$: 1) $x=0.0$; 2) $x=0.005$; 3) $x=0.01$.

The temperature dependence of the electrical conductivity of $Gd_xSn_{1-x}Se$ crystals is shown in Figure 3. As can be seen from the graphs plotted on the scale $\sigma \propto f(10^3/T)$, the value of electrical conductivity (σ) at a given temperature proportionally decreases upon moving from the $SnSe$ compound to solid solutions based on it. On the other hand, the $\sigma(T)$ dependence changes according to a law close to exponential. In the temperature range $T = 300 \div 400K$, the electrical conductivity changes according to a weak and monotonic law. In the temperature range $T = 400 \div 480K$, the σ value remains relatively constant. At $T \geq 420K$, the graph passes through a minimum and partially increases, and at $T = 560K$, a monotonic, sharper increase occurs again. In the sample with composition $x = 0.01$, this anomalous change is partially weak, and at temperature $T > 620K$ the change in $\sigma(T)$ occurs with the same intensity in both compositions.

For the studied samples, the thermal activation energy of charge carriers was determined. It was found that in the temperature range $T = 300 \div 400K$ in sample 2, containing $x = 0.005$: $E_A = 0.27 eV$, and for sample 3 ($x = 0.01$) $E_A = 0.02 eV$ [18].

On the other hand, the strengthening of the $\sigma(T)$ dependence at temperatures $T > 500K$ indicates that "heavy" charge carriers also participate in conductivity due to the activation of additional impurity energy levels located deep [19].

3.3. Hall coefficient in solid solutions $Gd_xSn_{1-x}Se$

The temperature dependence of the Hall coefficient of the obtained samples of the composition ($x = 0.0, 0.005$ and 0.01) was studied and the results are presented in Figure 4. As can be seen from the graphs, the temperature dependence of the Hall coefficient $R(T)$ corresponds to the dependence of electrical conductivity $\sigma(T)$. As in the electrical conductivity mechanism, the Hall coefficient in the region of impurity conductivity is weak, monotonically decreasing. This decrease corresponds to an increase in the concentration of charge carriers as a result of thermal excitation with increasing temperature. With a subsequent increase in temperature, the Hall coefficient increases. This anomaly is explained by the presence of traps in

the forbidden zone for electrons or the formation of additional acceptors with an increase in temperature [20].

With a subsequent increase in temperature ($T > 560K$), it passes through a weak extremum, sharply decreases and approaches the temperature characterizing the intrinsic conductivity. The decrease in the $R(T)$ dependence, although insignificant, after passing the extremum, shows that the band structure of these samples is complex. This type of dependence is found in the base compound $SnSe$, as well as in its structural analogs. The reason for this is the complex nature of the band structure of these compounds, the state of the valence band from two lower bands and is explained by the existence of light and heavy holes, respectively.

In the presence of light and heavy holes, due to the weak dependence of the ratio of their mobility on temperature, the temperature dependence of the Hall coefficient is determined by the distribution of charge carriers in the valence subbands. Due to the weak mobility of holes in the second valence band, their share in the Hall effect is weak, due to the passage of holes into the second zone, the effective concentration decreases, and the Hall coefficient increases.

Experiments show that the electrical conductivity and Hall coefficient of the samples in the temperature range of our study change according to the regularity of semiconductor materials. Depending on the sign of the thermo EMF and the Hall coefficient in the samples, it was found that at room temperature the sample with the content of $x = 0.005$ has p -type conductivity, and the sample with the content of $x = 0.01$ has n -type conductivity. The Hall coefficient of the sample with the composition $x = 0.005$ changes sign from positive to negative at a temperature of $T = 455 K$. With a further increase in temperature, the sign of the Hall coefficient becomes negative.

A change in the sign of the Hall coefficient when passing the inversion point can occur for two reasons. The first reason: due to an increase in temperature due to the activation of charge carriers at partially localized energy levels, the concentration of electrons can increase, and in the second case this can be due to the high mobility of electrons participating in conductivity. The obtained sample compositions are partially compensated semiconductor materials; three types of charge carriers participate in conductivity simultaneously.

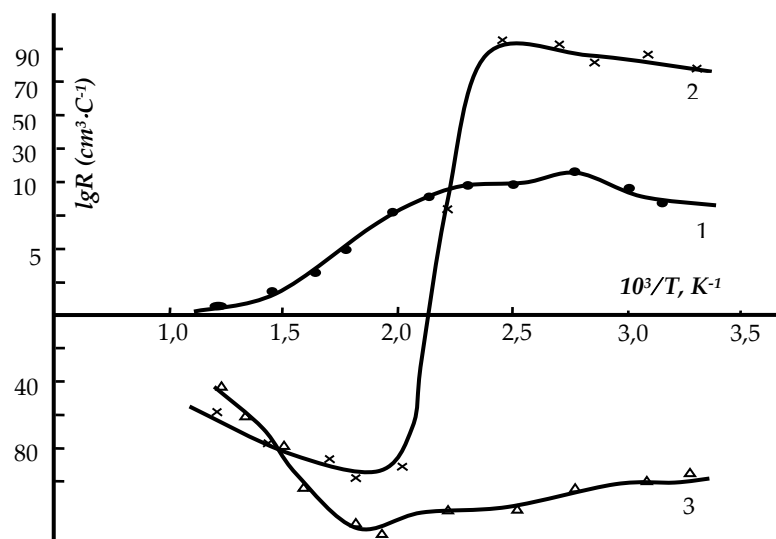


Fig. 4. Temperature dependence of the Hall coefficient in solid solutions $GdxSn_{1-x}Se$: 1) $x=0,000$; 2) $x=0,005$; 3) $x=0,010$

The temperature dependence of the Hall coefficient for the sample with $x = 0.01$ is shown on the 3rd curve. This sample has n -type conductivity, and the absolute value of the Hall coefficient slightly increases with temperature. It decreases, passing through a weak maximum at $T = 525K$. Such an anomalous change in the $R(T)$ dependence can occur for two reasons. The first reason can be associated with the depletion of the number of free electrons participating in conductivity from donor energy levels at this temperature ($T = 525K$), and the second reason can be associated with the complex structure of the energy band. The complexity of the band structure leads to the fact that excited electrons at this temperature become "heavy" electrons and create exciton pairs. For this reason, the value of the total electrical conductivity decreases. The temperature dependence of the Hall coefficient $R(T)$ indicates that the scattering of charge carriers from different centers is quite complex [21].

3.3. Magnetoresistance in $Gd_xSn_{1-x}Se$ solid solutions

Figure 5 shows the temperature dependence of the magnetoresistance of the $Gd_xSn_{1-x}Se$ melt system ($x = 0; 0.005; 0.01$). As can be seen from the graph, magnetic resistance is observed in all the studied samples and at a temperature of $T = 300K$ $\Delta\rho/\rho$ has a maximum value. With increasing temperature, due to the $(\Delta\rho/\rho_0)$ of charge carriers of the second kind, i.e., minor charge carriers, and their change in the magnetic field, is the cause of a different increase in magnetic resistance.

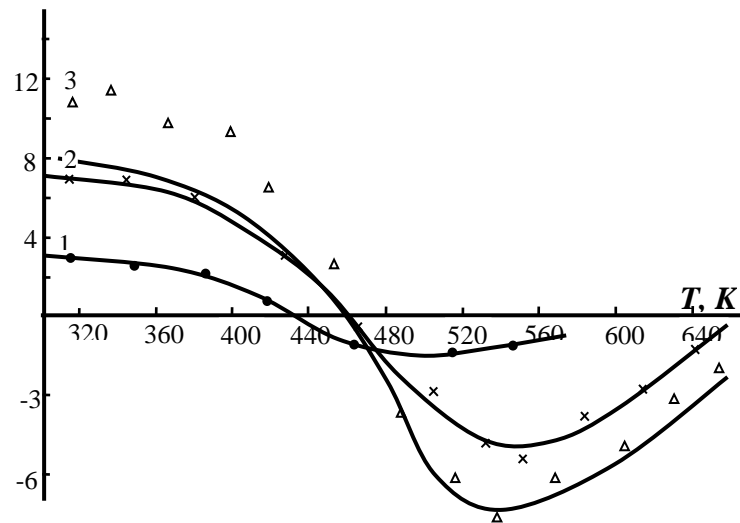


Fig.5. Temperature dependence of the change in the relative magnetoresistance of the solid solution of the $Gd_xSn_{1-x}Se$ system: 1- $x=0.0$; 2- $x=0.005$; 3- $x=0.01$ 1) $x=0,000$; 2) $x=0,005$; 3) $x=0,010$

The magnetic resistance in the binary compound $SnSe$ at room temperature is 3%. With increasing temperature, the absolute value of the magnetic resistance decreases and after 420 K, having performed an inversion, changes sign from positive to negative (Figure 3, curve 1). With an increase in the amount of Gd element in the composition, the absolute value of magnetic resistance ($\Delta\rho/\rho$) increases, but its temperature dependence changes similarly to a binary compound.

The inversion points in solid solutions of $SnSe$ with the element Gd shifts to the region of higher temperature: for samples of composition $x = 0.005$ the inversion point occurs at temperature $T = 460K$; and for samples of composition $x = 0.01$ at temperature $T = 470K$. As a

result, due to activation of charge carriers of the second kind, the magnetic resistance created by them is of great importance.

With further increase in temperature the sign of $(\Delta\rho/\rho)$ is negative and in the temperature range $T = 530 - 560K$, having passed through the maximum, decreases. The change in the sign of magnetic resistance in this temperature range also shows a change in the mechanism of scattering of charge carriers. A large absolute value of $(\Delta\rho/\rho)$ shows the presence of charge carriers of the second kind in the composition [22].

Thus, it was determined that the change in the mechanism of scattering of charge carriers also involves carriers of the second kind of this composition. The dependence of the magnetic resistance on the magnetic field strength (H) near this inversion point at a temperature of $T = 420 K$ was investigated (Fig. 6).

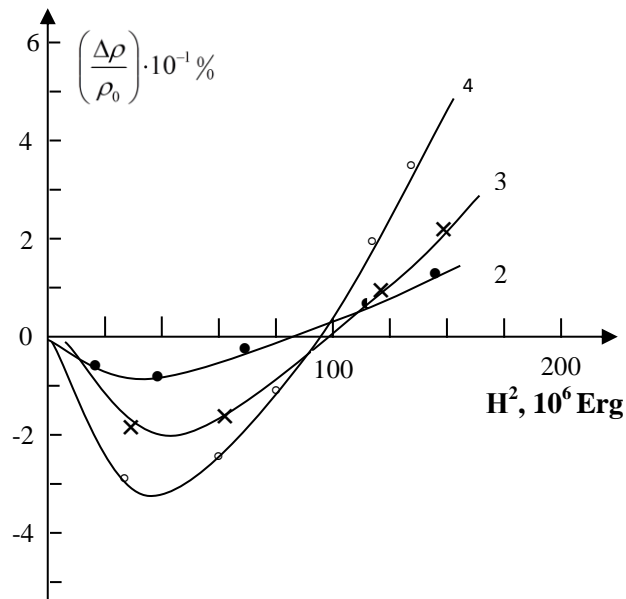


Fig.6. Dependence of the magnetoresistance of $Gd_xSn_{1-x}Se$ on the magnetic field strength:
2- $x=0.005$; 3- $x=0.01$; 4- $x=0.02$.

The dependence of the magnetoresistance on the magnetic field strength is given in the coordinates $(\Delta\rho/\rho) = f(H^2)$. It is evident from the figure that the magnetic resistance $(\Delta\rho/\rho)$ does not change linearly from the magnetic field strength. This is explained by the expenditure of additional energy on the direction of spin ordering of "light" and "heavy" electrons.

The study of the dependence of magnetic resistance on the magnetic field strength shows that at low values of the magnetic field strength in the direction of the field H , energy is spent on the direction of spin ordering of both free and localized microcenters. Due to the increase in the magnetic field strength and spin, the number of shared electrons increases, and then at a certain value of H , the magnetic resistance increases linearly [23].

At a relatively large field value, with an increase in H , the increase in the number of shared electrons along the spin is observed linear dependence $\Delta\rho/\rho = f(H^2)$. Here there is a probability of the transition of partially localized microferromagnetic centers to paramagnetic ones.

From the analysis of the literature, it was determined that if magnetic resistance and its change are observed in these samples, then such substances have a complex structure of the

energy band. In general, the observation of an arbitrary composition of magnetic resistance and its high value shows both the complex structure of the energy band of the substance and the presence of charge carriers of the second kind. Due to the activation of charge carriers of the second kind, the emergence of a large value of magnetic resistance in the samples is observed.

4. Conclusion

The results of the complex physicochemical analyses show that the dissolution region of $GdSe$ in $SnSe$ at room temperature is limited to 2 mol%. The $Gd_xSn_{1-x}Se$ alloy system, like the main substance $SnSe$, crystallizes in the orthorhombic syngony. With an increase in the percentage of $GdSe$ in the composition, a slight increase in the parameters of the unit cell of the crystal lattice, density and microhardness is observed, and thermal effects shift to the region of relatively lower temperatures.

In solid solutions of $Gd_xSn_{1-x}Se$, impurities are compensated by intrinsic defects, with moderate compensations, the concentrations of current carriers decrease accordingly and with an increase in the concentration of gadolinium in solid solutions ($x = 0.005$), a change in the sign of p to n type conductivity is observed. From the dependence $\sigma(T)$, the activation energies of levels located in the forbidden zone are determined, approximately 0.2 eV below the bottom of the conduction band, and the degree of compensation slightly affects the activation energy. Filling of tin vacancies and change of chalcogen antistructural defects leads to decrease of specific conductivity, concentration of charge carriers, activation energy and width of forbidden zone. Temperature dependence of Hall coefficient is well explained on the basis of two-zone model.

As temperature increases, absolute value of magnetic resistance decreases and inversion changes sign from positive to negative. As amount of Gd element in composition increases, absolute value of magnetic resistance increases and inversion point shifts to the region of higher temperature. From magnetic field dependences of resistance in $Gd_xSn_{1-x}Se$ samples, it follows that magnetoresistance of samples is typical for semiconductors, in weak magnetic fields standard, quadratic growth is observed.

REFERENCES

- [1] Shi W., Gao M., Wei J., Gao J., Fan C., Ashalley E., Li H., Wang Z. Tin selenide ($SnSe$): growth, properties, and applications. *Adv. Sci.*, 5 (4) (2018), p. 1700602; DOI: 10.1002/advs.201700602
- [2] Zhou Y., Li W., Wu M., Zhao L.D., He J., Wei S.H., Huang L. (2018 Jun 8) Influence of defects on the thermoelectricity in $SnSe$: A comprehensive theoretical study. *Phys. Rev. B*, 97 (24), Article 245202; DOI: 10.1103/PhysRevB.97.245202
- [3] Dar M.A., Govindarajan D., Batoor K.M., Hadi M., Dar G.N. (2022) Photovoltaic and Supercapacitor performance of $SnSe$ nanoparticles prepared through co-precipitation method. *Mater. Technol.*, 37 (10), pp. 1396-1409; DOI: 10.1080/10667857.2021.1950887
- [4] Kaur G., Vij A., Kumar A., (2022) Recent Advances in Earth Abundant and Environmentally Green Semiconducting Chalcogenide Nanomaterials for Photovoltaics Applications. *Advanced Nanomaterials*. 21-50. https://doi.org/10.1007/978-3-031-11996-5_2
- [5] Li Z., Guo Y., Zhao F., Nie C., Li H., Shi J., Liu X., Jiang J., Zuo S. (2020) Effect of film thickness and evaporation rate on co-evaporated $SnSe$ thin films for photovoltaic applications. *RSC Adv.*, 10 (28), pp. 16749-16755, DOI:10.1039/D0RA01749C

- [6] Assili K., Gonzalez O., Alouani K., Vilanova X. (2020) Structural, morphological, optical and sensing properties of SnSe and SnSe₂ thin films as a gas sensing material. *Arab. J. Chem.*, 13 (1), pp. 1229-1246, DOI: 10.1016/j.arabjc.2017.10.004
- [7] Li Z., Ding J., Mitlin D. (2015) and tin compounds for sodium ion battery anodes: phase transformations and performance. *Acc. Chem. Res.*, 48 (6), pp. 1657-1665; DOI: 10.1021/acs.accounts.5b00114
- [8] JAGANI H.S., DIXIT V., PATEL A., GOHIL J., PATHAK V. M. (2022) **STABILITY & DURABILITY OF SELF-DRIVEN PHOTO-DETECTIVE PARAMETERS BASED ON SN_{1-B}SB_BSE (B = 0, 0.05, 0.10, 0.15, 0.20) TERNARY ALLOY SINGLE CRYSTALS.** *RSC ADV.*, 12, 28693- 28706; DOI: 10.1039/D2RA05492B
- [9] Burton M.R., Boyle^{C.A.}, Liu T., et.al. (2020) Full Thermoelectric Characterization of Stoichiometric Electrodeposited Thin Film Tin Selenide (SnSe). *ACS Appl Mater Interfaces*;12(25):28232-28238; DOI: 10.1021/acsami.0c06026
- [10] Shi W., Gao M., Wei J., Gao J. (2018) Tin Selenide (SnSe): Growth, Properties, and Applications. *Advanced Science*, 5(4):1700602; DOI:10.1002/advs.201700602
- [11] Kumar M., Rani S., Singh Y., Gour K.S. (2021) Tin-selenide as a futuristic material: properties and applications.; 11(12):6477-6503; DOI:10.1039/d0ra09807h
- [12] ALIEV I.I., HUSEYNOV J.I., MURGUZOV M.I., ISMAILOV SH.S., GOJAEV E.M. (2014), PHASE RELATIONS AND PROPERTIES OF ALLOYS IN THE SNSE-DYSE SYSTEM. *INORG MATER* 50, 237–240. [HTTPS://DOI.ORG/10.1134/S0020168514030029](https://doi.org/10.1134/S0020168514030029)
- [13] Huseynov J.I., Murguzov M.I., Ismayilov S.S., (2013) Specific features of self-compensation in Er_xSn_{1-x}Se solid solutions. *Semiconductors* 47, 323–326. <https://doi.org/10.1134/S106378261303010X>
- [14] Huseynov D.I., Murguzov M.I., Ismailov S.S., (2008) Thermal conductivity of Er_xSn_{1-x}Se (x ≤ 0.025) solid solutions. *Inorg Mater* 44, 467–469. <https://doi.org/10.1134/S0020168508050063>
- [15] Ismailov Sh.S., Huseynov J.I., Musaev M.A., Abbasov I.I., Abdurakhmanova V.A. (2020) Effect of doping level and compensation on thermal conductivity in Ce_xSn_{1-x}Se solid solutions. *Low Temp. Phys.* 46, 1114–1120; <https://doi.org/10.1063/10.0002155>
- [16] Huseynov J.I., Murquzov M.I., Mamedova R.F., Ismailov Sh.S. (2008) Thermal Conductivity and Termal EMF of Materials for Thermal Energy Converters // TPE-06 3rd Intern. Conf. on Technical and Physical Problems in Power Engineering, Ankara.
- [17] Huseynov J.I., Jafarov T.A., (2012) Effect of γ-ray radiation on electrical properties of heat-treated Er_xSn_{1-x}Se single crystals. *Semiconductors* 46, 430–432. <https://doi.org/10.1134/S1063782612040082>
- [18] Abbasov I., Musayev M., Huseynov J. (2022) et al. Temperature behavior of X-Ray luminescence spectra of ZnSe // *International Journal of Modern Physics B*, Vol. 36, No. 02, 2250018 ; <https://doi.org/10.1142/S0217979222500187>
- [19] Abbasov I.I., Musayev M.A., Huseynov C.I., et at. A study of impurity defect photoluminescence in ZnSe:Cr and ZnSe:Fe in the near infrared at room temperature. *Advanced Physical Research*, 5(3), 192-199, (2023);
- [20] Dashdemirov A.O., Huseynov J.I., Rzayev R.F., Aliyev Y.I. (2022), Thermophysical behavior in Y₂O₃ under high intensity fast neutron irradiation *Modern Physics Letters B*, Vol. 36, No. 20, 2250092 ; <https://doi.org/10.1142/S0217984922500920>
- [21] Ismailov Sh.S., Huseynov J.I., Musaev M.A., Abbasov I.I., Abdurakhmanova V.A. (2020) Effect of doping level and compensation on thermal conductivity in Ce_xSn_{1-x}Se solid solutions // *Low Temp. Phys.* 46, 1114–1120; <https://doi.org/10.1063/10.0002155>
- [22] Hasanov K.A., Huseynov J.I., Dadashova V.V. (2016) et al. Effect of Phonon Drag on the Thermopower in a Parabolic Quantum Well. *Semiconductors* 50, 295–298. <https://doi.org/10.1134/S106378261603009X>
- [23] Huseynov D.I., Murguzov M.I., Ismailov S.S., (2008), Thermal conductivity of Er_xSn_{1-x}Se (x ≤ 0.025) solid solutions. *Inorg Mater* 44, 467–469. <https://doi.org/10.1134/S0020168508050063>

UOT 536.77:547.442

DOI: <https://doi.org/10.30546/09081.2024.102.7084>

SUMMARY OF EXPERIMENTAL DATA ON THE DENSITY AND VISCOSITY OF "ILISU SANGAR" AND "ILISU BESHBULAG" THERMAL WATERS IN THE GAKH DISTRICT OF AZERBAIJAN

M.M. BASHIROV¹, N.D. NABIYEV¹, N.S.RZAYEV¹, A.N. NAMAZOVA²

¹Baku Engineering University,

²Technical-Humanitarian Lyceum,

Baku / AZERBAIJAN

mbashirov@beu.edu.az, nnabiyev@beu.edu.az, nrzayev@beu.edu.az

ARTICLE INFO	ABSTRACT
<p>Article history: Received: 2025-02-07 Received in revised form: 2025-02-20 Accepted: 2025-02-25 Available online</p> <hr/> <p>Keywords: <i>thermal waters, renewable energy sources, dynamic viscosity, kinematic viscosity, density.</i></p>	<p><i>This study presents a comprehensive analysis of experimental data on the density, dynamic viscosity, and kinematic viscosity of the thermal waters of "Ilisu Sangar" and "Ilisu Beshbulag," located in the northern region of the Gakh district in the Republic of Azerbaijan. The experiments on the density, dynamic viscosity, and kinematic viscosity of the thermal waters were conducted using advanced instrumentation manufactured in Germany. The densities of the "Ilisu Sangar" and "Ilisu Beshbulag" thermal waters were precisely quantified using the "Anton-Paar SVM-300 Stabinger" viscometer, while their dynamic viscosities were determined with high precision utilizing the DMA 5000 M apparatus. Using the experimental data of $p=f(u)$ and $p=f(v)$ at selected temperatures, analytical dependences of thermal waters were derived. The obtained values are described by polynomial equations. Polynomial equations enable the calculation of the experimental density values of the "Ilisu Sangar" and "Ilisu Beshbulag" thermal waters in the Gakh district at various temperatures, with a maximum error margin of $\pm 0.25\%$.</i></p>

1. Introduction

Adoption of alternative energy sources has become increasingly prevalent in both developed and developing nations. This transition is primarily driven by the imperative for environmental sustainability and the objective to minimize the harmful waste emissions into the ecosystem. Furthermore, there is an escalating demand for alternative energy sources as substitutes for conventional ones. Although the economic costs associated with renewable energy sources are generally higher than those of non-renewable sources, efforts are being made to enhance their economic viability. In pursuit of this, the United Nations and various international organizations have implemented a range of policies aimed at promoting the utilization of renewable energy. Consequently, Azerbaijan has fostered considerable opportunities for the advancement and utilization of alternative energy sources.

Azerbaijan has a favorable geographical position for utilizing thermal waters. The country can harness the energy from 172 million m³ of geothermal waters, with temperatures ranging from 40 to 100°C, year-round.

Solar energy is regarded as an economically viable solution for heating administrative and residential buildings, warming greenhouses, and processing agricultural products.

On a local scale, both biomass and geothermal energy are actively utilized. In an effort to enhance the deployment of alternative energy sources, drawing upon global best practices, the President signed Decree No. 4 on November 24, 2003. The preparation of the document on the use of these energy sources was entrusted to the Ministries of Ecology and Natural Resources, Economic Development, Fuel and Energy, as well as the Azerbaijan National Academy of Sciences (ANAS).

To gain from global experience, the Republic of Azerbaijan became a member of the International Renewable Energy Agency, which was established on June 10, 2009. This initiative will be carried out continuously, as outlined in Decree No. 182, signed by the President of the Republic of Azerbaijan in November 2009 [1].

The State Program advocates for the development and implementation of regulatory and legal frameworks to facilitate the utilization of alternative energy sources in the Republic of Azerbaijan. Engaging private investors in the preparation of projects is essential for the successful deployment of alternative and renewable energy sources. This involvement will ensure the efficient operation of these projects under optimal conditions and foster the integration of environmentally sustainable energy solutions into the energy market.

The action plan also encompasses public education on alternative and renewable energy sources, alongside the development and dissemination of educational materials in this field. Currently, various higher education institutions in Azerbaijan are effectively undertaking these initiatives.

To attract investors with international expertise, the Ministry of Energy and Industry has engaged specialists in consultations with international institutions, embassies, global organizations, and foreign enterprises. These efforts aim to acquire valuable insights for the effective implementation of this State program and to facilitate the invitation of foreign investors to participate in initiatives within Azerbaijan [1].

Azerbaijan is endowed with a substantial reserve of mineral waters, with more than 1,000 natural springs distributed across the country. These springs are predominantly located in the mountainous regions, which are characterized by a high concentration of natural water sources. The extraction of mineral waters is typically conducted through drilling. Azerbaijan has a highly diverse and complex relief structure from a physical and geographical perspective.

Approximately 90% of Azerbaijan's natural mineral water sources, totalling 905, are located in mountainous regions, while the remaining 10%, or 98 sources, are found in flat, plain areas. The composition of mineral water, determined by the concentration of various elements by weight, is chemically highly active. Unlike ordinary water, mineral waters contain dissolved gases, salts, and trace elements. The physical and chemical properties, as well as the quality of the mineral waters, vary depending on the types and concentrations of elements present.

The temperature of mineral waters in Azerbaijan varies between 4 and 65°C. This applies only to natural water sources. In addition, waters reaching 95°C are extracted by drilling deep into the earth in Azerbaijan.

In our republic, there are high-temperature mineral waters—Donuzutan (64°C in Masalli) and Istisu (62°C in Kalbajar). Waters with a temperature of 35-36°C are more valuable due to

their temperature characteristics. This temperature closely matches that of the human body, giving these waters significant therapeutic benefits.

This type of water can be found in Khaltan (in the Shabran district), Ilisu (in the Gakh district) (36⁰-42⁰C) etc.

Problem statement. Among geothermal energy resources, the Ilisu spring group, located within the Sheki-Zagatala economic-geographical region (figure 1), is particularly well-known. Situated in the northwestern part of Azerbaijan, the Gakh administrative district is distinguished not only by its other natural advantages but also by the abundance of its thermal and mineral waters. The Ilisu thermal water groups, known for their hydrosulfide and hydro carbonate properties, along with the mineral waters found on both banks of the Gurmukh River near the village of Alibeyli and in the Qaynama area, hold significant potential for resort and tourism development. However, these resources remain underutilized. The Ilisu mineral water group operates 10 outlets and consists of hydrosulfide waters containing sodium bicarbonate (NaHCO₃). This mineral water has been used for therapeutic purposes by the local population since ancient times. The names of the two main springs—Oglan-Bulag (for men) and Qız-Bulag (for women), confirm this.



Fig.1. Map of the thermal and mineral water resources in the Sheki-Zagatala economic-geographical region.

The thermal energy resources of the Gakh administrative district, which is part of the studied Sheki-Zagatala economic-geographic region, are particularly valuable. As such, their diverse chemical composition, high healing properties, and favorable geographical location of the area create a good basis for their wide application for therapeutic purposes and in various sectors of the national economy [2]. The experimental study of the thermal properties of water, specifically its (viscosity and density), in this administrative region is highly relevant. The viscosity (internal friction) of liquids and gases is one of the most important transfer properties. To accurately calculate flow rate, velocity, and pressure drop, it is essential to know the dynamic viscosity coefficient. Additionally, viscosity plays a crucial role in determining heat exchange in

both liquids and gases, as it influences both free and forced convection. The viscosity coefficient is a key component in several important criteria (modules), including Reynolds, Prandtl, Rayleigh, and Stanton numbers.

The coefficient of viscosity plays a significant role in the molecular-kinetic theory of liquids and real gases. It is well-established that the most accurate viscosity information is obtained through experimental methods. Various techniques have been proposed for measuring viscosity, and new viscometer designs have been developed. Additionally, existing viscometers have been modernized, and formulas for calculating viscosity have been refined.

The geographical coordinates of the "Ilisu Sangar" and "Ilisu Beshbulag" thermal springs in the Gakh administrative district, along with the temperatures of these waters at the point of emergence, are presented in Table 1.

Table 1. The geographical coordinates of the Gakh thermal springs and their temperatures at the point of emergence from the source.

The name of the source	Geographical coordinates	Temperature at the point of emergence
"Ilisu Sangar"	41°28'05" North 47°03'37" East	T=305,15 K
"Ilisu Beshbulag"	41°27'58" North 47°03'50" East	T=303,15 K

Purpose of the study. It consists of an analytical summary of the experimental results of the density, dynamic and kinematic viscosity of the thermal waters of the "Ilisu Sangar" and "Ilisu Beshbulag" thermal waters of the Gakh district of the Republic of Azerbaijan at different temperatures.

2. Problem-solving approach.

Extensive experimental studies have been carried out over several years to accurately examine the density, dynamic viscosity, and kinematic viscosity of the thermal waters in the Gakh administrative district of the Republic of Azerbaijan, specifically at "Ilisu Sangar" and "Ilisu Beshbulag." The results of these studies have been published in esteemed scientific journals both nationally and internationally [3-9].

The thermal waters under investigation were collected directly from their surface sources and processed for experimental analysis using various chemical methods. To measure density under atmospheric pressure, a high-precision DMA 5000 M instrument from the Anton Paar series was used [10]. The density measurements of the liquids were conducted at temperatures ranging from $T = 278.15 \text{ K}$ to 343.15 K and at a pressure of $p = 0.101 \text{ MPa}$. To determine the dynamic viscosity, the **German-made SVM3000 Stabinger viscometer** was utilized. This instrument offers an exceptionally broad range of measurement capabilities in terms of viscosity and temperature.

The experiments were conducted at atmospheric pressure and temperature $T = (278.142 \div 373.150) \text{ K}$ and it is also possible to calculate the kinematic viscosity in $\left(\nu, \frac{m^2}{s} \right)$ by using

the equation $\nu = \frac{\mu}{\rho}$ (1). Here, μ represents the dynamic viscosity (Pa·s), and ρ denotes the density (kg/m^3).

The experimental values of density (ρ), dynamic viscosity (μ), and kinematic viscosity (ν) of the "Ilisu Sangar" and "Ilisu Beshbulag" thermal waters in the Gakh administrative district of the Republic of Azerbaijan are presented in Tables 2 and 3.

Table 2. The experimental values of the density of the "Ilisu Sangar" and "Ilisu Beshbulag" thermal waters at various temperatures in the Gakh administrative district of the Republic of Azerbaijan.

"Ilisu Sangar"		"Ilisu Beshbulag"	
T/K	ρ / kg/m ³	T/K	ρ / kg/m ³
278.16	1000.40	278.15	1000.56
283.14	1000.12	283.14	1000.18
293.14	998.71	293.14	998.64
298.15	997.61	298.14	997.50
303.15	996.27	303.15	996.12
313.14	992.90	313.14	992.73
323.15	988.68	323.15	988.55
333.16	983.71	333.15	983.67
343.15	978.12	343.16	978.19

Table 3. The experimental values of dynamic viscosity μ (Pa·s) and kinematic viscosity ν ($\frac{m^2}{s}$) at various temperatures of "Ilisu Sangar" and "Ilisu Beshbulag" thermal waters in the Gakh administrative district of the Republic of Azerbaijan.

"Ilisu Sangar"			"Ilisu Beshbulag"		
T/K	$\mu \cdot 10^6$	$\nu \cdot 10^6$	T/K	$\mu \cdot 10^6$	$\nu \cdot 10^6$
278.147	1549.52	1.5489	278.148	1526.15	1.5253
283.148	1348.26	1.3481	283.148	1325.24	1.3250
293.151	1052.64	1.0540	293.154	1031.39	1.0328
298.155	943.93	0.9462	298.151	924.88	0.9272
313.151	697.01	0.7020	313.152	694.91	0.7000
333.151	502.68	0.5110	333.150	519.38	0.5280
343.151	435.26	0.4450	343.150	461.71	0.4720
353.150	382.96	0.3940	353.152	417.08	0.4290
363.150	339.81	0.3520	363.150	382.85	0.3964
373.150	305.74	0.3190	373.150	355.06	0.3702

Based on the experimental results for the thermal waters studied at the same temperature, the data were analyzed in the ρ - μ and ρ - ν coordinate systems using the polynomial equations presented in equations (2) and (3). The article highlights the derived relationships and key findings $\rho = f(\mu)$ $\rho = f(\nu)$ from this analysis.

$$\rho = \sum_{i=0}^3 a_i \cdot \mu^i \quad (2)$$

$$\rho = \sum_{j=0}^2 b_j \cdot \nu^j \quad (3)$$

Here, a_i and b_j represent the polynomial coefficients determined from the experimental data through the least squares regression method and are provided in Table 4.

Table 4. The values of coefficients a_i and b_i obtained from equations (2) and (3) for the thermal waters of "Moksu," "Ilisu Sangar," and "Ilisu Beshbulag" in the Gakh district of the Republic of Azerbaijan.

"Ilisu Sangar"	"Ilisu Beshbulag"
a_i	a_i
$0.926312506572 \cdot 10^3$	$0.905605233673 \cdot 10^3$
0.172757438379	0.241573032787
$-0.136742202183 \cdot 10^{-3}$	$-0.206702661061 \cdot 10^{-3}$
$0.362714422921 \cdot 10^{-7}$	$-0.206702661061 \cdot 10^{-3}$

“Ilisu Sangar”	“Ilisu Beshbulag”
b_j	b_j
$0.923496875591 \cdot 10^3$	$0.912248432340 \cdot 10^3$
$0.179754846953 \cdot 10^3$	$0.211873411334 \cdot 10^3$
$-0.142463926142 \cdot 10^3$	$-0.172041331853 \cdot 10^3$
$0.378093573540 \cdot 10^2$	$0.466817289082 \cdot 10^2$

3. Conclusion

Considering equations (2) and (3) along with the polynomial coefficients provided in Table 4, it is possible to calculate the density values of the thermal waters from the “Ilisu Sangar” and “Ilisu Beshbulag” thermal springs located in the Gakh district of the Republic of Azerbaijan at various temperatures. The maximum error in these calculations is $\pm 0.25\%$. Furthermore, equations (2) and (3) enable us to derive both extrapolated and interpolated density values of the thermal waters from the “Ilisu Sangar” and “Ilisu Beshbulag” springs at different temperatures.

REFERENCES

1. Decree of the President of the Republic of Azerbaijan on the Approval of the Statute of the State Agency for Alternative and Renewable Energy Sources under the Ministry of Industry and Energy of the Republic of Azerbaijan, Baku, November 10, 2009.
2. Namazova A.M. Economic importance of mineral and thermal waters of the Sheki- Zagatala economic-geographical region // Baku University News. Natural Sciences Series, 2015, No. 3, p. 152-159
3. Ahmadov A.I. Chemical analysis of geothermal waters of Gakh and Gabala regions of Azerbaijan. Azerbaijan Technical University. Scientific Works vol. 1, №4, Baku-2013.
4. Ahmadov A., Safarov J., Bashirov M., Hassel E. Thermo physical properties of north-west Azerbaijan geothermal waters. Azerbaijan Technical University “Thermophysical and mechanical properties of advanced materials”.
5. Ahmadov, A.I. Chemical Analysis of Geothermal Waters in the Gakh and Gabala regions. *Proceedings of the Republic Scientific Conference on Heydar Aliyev and Education in Azerbaijan*, Azerbaijan Technical University, May 7–8, 2013.
6. Ahmadov, A.I., Bashirov, M. Thermal-physical properties of geothermal waters in the Gakh and Gabala regions. *“Proceedings of the I International Conference of Young Researchers” dedicated to the 90th Anniversary of the National Leader Heydar Aliyev*, Qafqaz University, April 25–26, 2013.
7. Ahmadov, A., Safarov, J., Bashirov, M., Hassel, E. Study of the viscosity of thermal waters in the Gakh and Gabala regions of Azerbaijan. *Journal of Qafqaz University: Physics*, volume 2, № 1. Baku-2014.
8. Ahmadov A., Safarov J., Bashirov M., Hassel, E. Saturated vapor pressure of thermal Waters in the Gakh and Gabala regions of Azerbaijan. *News of the Azerbaijan National Academy of Sciences. Institute of Physics and Astronomy*, Volume 34, №. 5, Baku-2014.
9. Ahmadov, A., Safarov, J., Klinov, A., Bashirov, M., Hassel, E. Experimental studies on the density of geothermal waters from the Gakh region of Azerbaijan over a wide range of pressures and temperatures. *Bulletin of Kazan Technological University*, T.18, №3, 2015.
10. R.Pippo. Geothermal Power Plants, Second edition, Principles, Applications, Case Studies and Environmental Impact, Butterworth-Heinemann; 2^d edition, 2008, 520 p.

UOT: 539.193/194

PACS: 11.15.-p

DOI: <https://doi.org/10.30546/09081.2024.102.7093>

SPATIAL STRUCTURES OF THE N-TERMINAL ANALOGUES OF NOCICEPTIN MOLECULE

Larisa ISMAILOVA, Simnara AKHMEDOVA*, Namiq AKHMEDOV

Baku State University, Institute for Physical Problems

* Azerbaijan Technical University

lara.ismailova.52@mail.ru, asimnara@mail.ru, namiqabdulavval@mail.ru

ARTICLE INFO	ABSTRACT
<p>Article history: Received: 2025-03-05 Received in revised form: 2025-03-17 Accepted: 2025-04-11 Available online</p> <hr/> <p>Keywords: nociceptin, structure, molecule, tripeptide, tetrapeptide, conformation.</p>	<p><i>This scientific work is devoted to study the spatial structure and conformational possibilities of the tripeptide Phe1-Gly2-Gly3 and tetrapeptide Phe1-Gly2-Gly3-Phe4 molecules. The knowledge of the structural and functional properties of these peptide molecules is of great practical importance for medicine and pharmacology. This neuropeptide molecules are stable analogues of the nociceptin molecule. The calculations were carried out by the method of theoretical conformational analysis with regard to nonvalent, electrostatic and torsional interactions, energy of the hydrogen bonds and a special computer program. The low-energy conformations of these molecules and the values of the dihedral angles of the main chains and side chains are found and the energy of the intra- and inter-residue interactions were estimated. 15 low-energy conformations were found for tripeptide for four spatial structures and 12 low-energy conformations were found for tetrapeptide for six spatial structures. It is revealed that low energy conformations of these molecules have the half-folded and folded type of backbone. The side chains of the Phe1 and Phe4 amino acids in low-energy conformations carry out effective interactions and are conformationally labile amino acids. They bring together sections of the main chain and side chains of amino acids that are part of the tri- and tetrapeptide, which leads to important interactions.</i></p>

1. Introduction

It is known, that new families of the regulatory peptides are being discovered and their properties are being studied. One of these families is nociceptins. For medicine and pharmacology, knowledge of the structure-functional properties of these peptide molecules is of great practical importance. Nociceptin is an opioid-related peptide with strong anti-analgetic properties. It is widely present in the central nervous system, affecting motor, anxiety and pain sensitivity. It is important to note that the original synthetic analogues of the N-terminal fragment of nociceptin, the tripeptide Phe1-Gly2-Gly3 (FGG) and tetrapeptide Phe1-Gly2-Gly3-Phe4 (FGGF). It causes the binding of natural nociceptin to a specific ORL1 receptor [1, 2].

More recently, new nociceptin analogues FGGF-GP, FGGF-PGP and FGGF-VGP have been synthesized. It has been shown that the FGGF-VGP peptide, like natural nociceptin, significantly reduces the level of locomotor activity of animals [3, 4]. The most pronounced effect of FGGF-GP was the anxiolytic effect. Our scientific work is devoted to study the spatial structure and

conformational possibilities of the tripeptide Phe1-Gly2-Gly3 and tetrapeptide Phe1-Gly2-Gly3-Phe4 molecules. It was found that the N-terminal tripeptide and tetrapeptide of this molecule are active [5, 6].

The short linear regulatory peptides in solutions do not have a fixed spatial structure. Usually, the amino acid sequence and physicochemical properties of the solvent determine the set of low-energy conformations of the peptide molecule. The biologically active conformation of this peptide molecule, which is realized upon interaction with the receptor molecule, is included in the set of low-energy structures. Therefore, the study of the spatial structure and conformational capabilities of peptide molecules is of great interest. The peptide molecules and their biological functions in living systems are related with their specific spatial structures. Therefore, to understand the mechanism by which the peptides function it is necessary to know their three-dimensional structures. It is important to know the full complement of low-energy conformational states.

The calculations were carried out by the method of theoretical conformational analysis with regard to nonvalent, electrostatic and torsional interactions, energy of the hydrogen bonds and a special computer program [7]. The low-energy conformations of this molecule and the values of the dihedral angles of the main chain and side chains are found and the energy of the intra- and inter-residue interactions was estimated. The present paper is an extension of our previous investigations of structural and functional organization of peptide molecules [8-19].

2. Materials and methods

Neuropeptides play an important role in all nervous systems and structure-functional studies of these peptides is one approach to understanding this role. The objects of our scientific research are the analogues of nociceptin molecule tripeptide Phe1-Gly2-Gly3 and tetrapeptide Phe1-Gly2-Gly3-Phe4. These molecules have the amino acid Gly, which has no side chain and amino acid Phe with large and labile side chain. Our calculations were carried out by the method of theoretical conformational analysis. The potential energy of these molecules were chosen as the sum of the nonvalent, electrostatic and torsional interaction energies and the energy of hydrogen bonds. Non-valent interactions were assessed using the Lennard-Jones potential. Electrostatic interactions were calculated in the monopole approximation according to Coulomb's law using partial charges on atoms. The conformational properties of these molecules were studied in an aqueous environment, and therefore the dielectric constant was taken to be 10. The energy of hydrogen bonds was estimated using the Morse potential.

In presenting the results of the calculation of the spatial structure of these molecules we used the classification suggested in the work [20]. All structural versions according to it break down into shapes including certain forms of the main chain, each form is represented by a set of conformations. The conformations are determined by the number of rotational degrees of freedom of the side chains of the residues being included in the molecule. The conformational state of each amino residue is conveniently described by the backbone φ , ψ , ω and side chain χ_1 , χ_2 ... dihedral angles. The terms "conformation" used in the following analysis will always imply exact quantitative characteristics of residue or fragment geometry. For a stable conformation, the φ and ψ dihedral angles are located in low-energy region R, B, L and P of the conformational map. We introduce the notion "form of a residue" to denote the region of its backbone dihedral angle. The conformation of the backbone forms of residue in a given amino acid sequence will

specify the backbone form of a fragment. Forms belonging to a particular shape have an analogous peptide chain contour and a similar mutual arrangement of backbones and side chains. Designations indications of dihedral angles have been measured up to the generally accepted nomenclature [21].

3. Results and Discussion

The three-dimensional structure and conformational possibilities of the tripeptide Phe1-Gly2-Gly3 and tetrapeptide Phe1-Gly2-Gly3-Phe4 molecules were determined based on the stable conformations of the mono-peptides. It is known that the active site of the nociceptin molecule that activates the receptor is the N-terminal tetrapeptide Phe1-Gly2-Gly3-Phe4 [5, 6].

The conformational properties of the tripeptide Phe1-Gly2-Gly3 were studied based on the stable conformations of the mono-peptides N-acetyl-L-phenylalanine and N-acetyl-L-glycine. For a given tripeptide containing 37 atoms and 10 variable dihedral angles, 4 shapes are possible (ee, ef, fe and ff), represented by 16 forms of the main chain. In total, about 100 conformations were calculated, all of them were minimized in energy, and their geometric and energy parameters were estimated. The calculation results are presented in Table 1. The geometric parameters of the four low-energy conformations of the tripeptide molecule are presented in Table 2.

The calculation revealed the presence of a sharp energy differentiation in the forms of the main chain and shapes. Just as in the experimental work [2], these conformations can represent four structures. The B₂₁BL conformation has the lowest energy ($U_{total} = -2.6$ kcal/mol), which belongs to the ef shape. This semi-folded shape is represented by the largest number of low-energy conformations - 12. In the global conformation of B₂₁BL ($\Delta U_{rel}=0$ kcal/mol), the energy of nonvalent interactions is -6.4 kcal/mol, electrostatic 2.3 kcal/mol and torsional 1.5 kcal/mol. The fully unfolded form of the main chain B₂₁BR (U_{total}

Table 1. The energy parameters: mono-peptide (U_1, U_2, U_3), di-peptide (U_{12}, U_{23}), tri-peptide (U_{13}) energies, relative energy (U_{rel}) and energy of nonvalent (U_{nv}), electrostatic (U_{el}) and torsion (U_{tors}) interactions of optimal conformations of tripeptide molecule

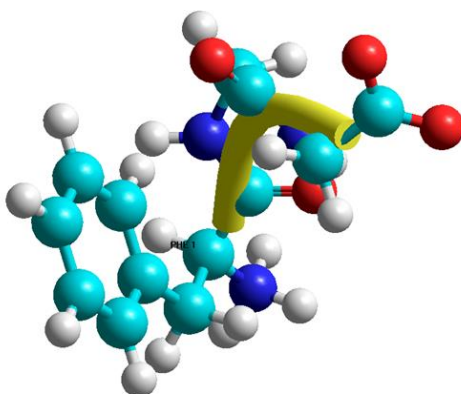
Nº	Shapes, conformations	U_1 mono-pep	U_2 di-pe	U_3 energy	U_{12} di-peptide	U_{23} energy	U_{13} tri-peptide	U_{nv}	U_{el}	U_{tors}	U_{rel}
1	ee B ₁₁ BB	0.6	1.3	1.6	-1.4	-0.4	-4.3	-5.5	2.6	1.6	1.3
2	B ₁₁ BR	0.6	1.3	1.6	-1.4	-0.4	-4.3	-5.6	2.6	1.6	1.2
3	B ₂₁ BB	0.8	1.3	1.6	-2.4	-0.3	-4.2	-6.0	2.7	1.5	0.9
4	B ₂₁ BR	0.7	1.3	1.6	-2.4	-0.3	-4.3	-6.2	2.7	1.5	0.6
5	B ₂₁ RL	0.6	1.3	1.5	-2.2	-0.5	-3.7	-5.6	2.8	1.4	1.3
6	R ₂₁ LB	1.3	1.2	1.5	-1.9	-0.3	-3.6	-6.1	3.3	1.7	1.1
7	ef B ₂₁ BL	0.7	1.3	1.6	-2.5	-0.2	-4.9	-6.4	2.3	1.5	0.0
8	B ₂₁ BP	0.8	1.3	1.6	-2.5	-0.3	-4.9	-6.3	2.3	1.7	0.3
9	B ₁₁ RB	0.6	1.3	1.6	-2.2	-0.6	-3.1	-5.2	2.5	1.4	1.4
10	B ₁₁ RR	0.6	1.3	1.7	-1.7	-0.7	-4.1	-5.3	2.4	1.4	1.1
11	R ₂₁ PR	1.2	1.3	1.6	-1.8	-0.4	-0.5	-6.1	3.2	2.1	1.7
12	fe B ₂₁ PL	0.6	1.2	1.6	-1.7	-0.4	-2.8	-4.0	2.6	1.5	2.8
13	ff B ₂₁ PB	0.6	1.2	1.5	-1.8	-0.3	-3.8	-4.4	2.0	1.5	1.7
14	B ₂₁ PR	0.7	1.3	1.6	-1.8	-0.3	-3.8	-4.4	2.0	1.6	1.8
15	R ₂₁ PL	1.3	1.3	1.6	-1.9	-0.3	-4.7	-6.1	3.3	1.7	1.5

Table 2. Geometric parameters (degree) of the optimal conformations of Phe-Gly-Gly tripeptide molecule

Residues	Shape (conformation)			
	ee (B ₂₁ BR)	ef (B ₂₁ BL)	fe (B ₂₁ PL)	ff (R ₂₁ PL)
Phe 1	-61 149 178 174 80	-59 153 180 180 86	-59 150 179 180 86	-56 -69 -177 170 73
Gly2	-83 69 180	-78 78 177	82 - 70 180	81 -69 180
Gly3	-93 -84 180	94 71 176	88 92 180	93 85 178
U _{rel} (kcal/mol)	0.6	0.0	2.8	1.5

Note: The values of dihedral angles are given in the sequence $\varphi, \psi, \omega, \chi^1, \chi^2, \dots$

= -2.0 kcal/mol) of the ee shape is inferior to it by only 0.6 kcal/mol. The conformations of the completely folded shape ff B₂₁PR (U_{total}= -0.6 kcal/mol) are low-energy. More than 3 kcal/mol is inferior to the conformation of another half-folded shape fe B₁₁PL (U_{total} = 0.4 kcal/mol). It should be noted that the main contribution to the energy of low-energy conformations is made by dipeptide and tripeptide interactions. The main energy contribution comes from nonvalent interactions. This contribution varies in the range from -1.1 to -7.0 kcal/mol. Figures 1(a, b, c, d) represent schematically the backbone forms and positions of residues in four low-energy conformations B₂₁BR (0.6 kcal/mol), B₂₁BL (0.0 kcal/mol), B₂₁PL (2.8 kcal/mol) and R₂₁PL(1.5 kcal/mol) of the tripeptide molecule Phe1-Gly2-Gly3 (table 2).



Figures 1a. Spatial structure of the low energy conformation B₂₁BR (0.6 kcal/mol) of the tripeptide molecule

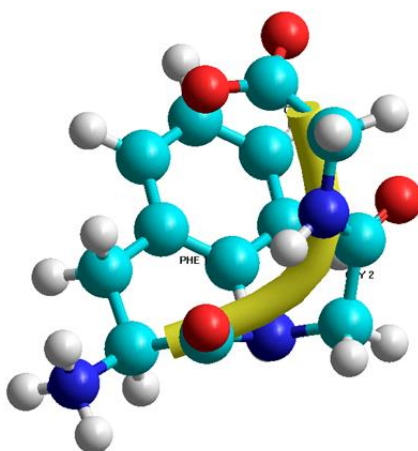


Figure 1b. Spatial structure of the low energy conformation B₂₁BL (0.0 kcal/mol) of the tripeptide molecule

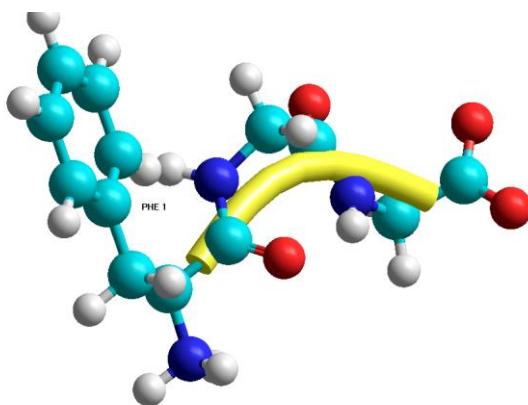


Figure 1c. Spatial structure of the low energy conformation B21PL (2.8 kcal/mol) of the tripeptide molecule

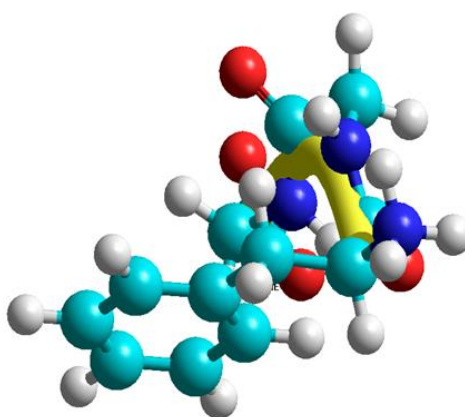


Figure 1d. Spatial structure of the low energy conformation R21PL (1.5 kcal/mol) of the tripeptide molecule

Figure 1b shows that in the global conformation B₂BL (0.0 kcal/mol) of the tripeptide molecule, the phenylalanine side chain hangs over the backbone of the two glycines. This promotes efficient di- and tripeptide interactions. In the case of a fully folded structure R₂PL (1.5 kcal/mol), the phenylalanine side chain is folded into the solvent and can interact with the receptor. All low-energy conformations of the tripeptide molecule were taken into account when calculating the structure of the tetrapeptide molecule Phe1-Gly2-Gly3-Phe4.

The amino acid sequence of the tetrapeptide molecule included two amino acids each phenylalanine and glycine. Tetrapeptide Phe1-Gly2-Gly3-Phe4 contains 57 atoms and 15 variable dihedral angles. The specificity of the amino acid side chains of the tetrapeptide molecule determined the number of initial approximations. In total, over 150 conformations were calculated, belonging to 64 forms of the main chain and 8 possible shapes for this molecule. All of them were minimized in energy, and their geometric and energy parameters were estimated. The calculation showed the presence of a sharp energy differentiation of conformations. Representatives of 22 forms of the main chain fall into the energy range 0 – 4 kcal/mol. The relative energy of the conformations of the tetrapeptide molecule varied within the range 0– 8 kcal/mol. There are the energy differentiation both in respect of the conformations, and forms of the main chain and shapes.

The low-energy conformations of the tetrapeptide molecule are presented in Table 3.

The global conformation of this molecule ($U_{rel}=0$ kcal/mol) is B₁₁RRR₁₁. The contribution of the stabilizing nonvalent to this conformation is (-14.6) kcal/mol, where as electrostatic interactions account for 2.6 kcal/mol and torsion for 1.9 kcal/mol. The main contributions of the interresidual interactions in this conformation were dipeptide contributions (-4.8) kcal/mol, tripeptide (-2.8) kcal/mol, tetrapeptide (-6.6) kcal/mol. In this conformation, amino acid residues Phe1-Gly2-Gly3-Phe4 form folded structure. The geometric parameters of this conformation of the tetrapeptide molecule are presented in Table 4. It is revealed that low energy conformations of this molecule have the folded and half folded types of backbone. These folded forms bring parts of the backbone and the side chains of the amino acids together, and they result in convenient interactions.

Table 3. The energy parameters: contributions of mono-peptide (U_1, U_2, U_3, U_4), dipeptide (U_{12}, U_{23}, U_{34}), tripeptide (U_{13}, U_{24}), tetrapeptide (U_{14}) energies, relative energy (U_{rel}) and energy contributions of nonvalent (U_{nv}), electrostatic (U_{el}), torsion (U_{tors}) interactions of optimal conformations of the tetrapeptide molecule

	Shapes, conformations	U_1	U_2	U_3	U_4	U_{12}	U_{23}	U_{34}	U_{13}	U_{24}	U_{14}	U_{nv}	U_{el}	U_{tors}	U_{rel}
1	eee B ₁₁ BBB ₁₁	-0.2	1.3	1.2	-0.3	-1.7	-0.2	-2.3	-3.0	-3.2	-1.5	-13.1	3.4	2.1	2.4
2	R ₂₁ PLB ₂₁	1.3	1.3	1.3	-0.3	-1.8	0.3	-2.8	-3.5	-1.6	-2.3	-12.3	4.0	2.2	4.1
3	efe B ₂₁ BLB ₁₁	-1.0	1.2	1.3	-0.3	-2.3	-0.3	-1.9	-2.6	-0.7	-6.1	-13.5	3.2	2.1	1.8
4	B ₂₁ BLR ₁₁	1.2	1.2	1.3	-0.2	-2.3	-0.3	-1.9	-2.6	-0.7	-6.0	-13.2	3.2	2.0	2.1
5	eff B ₁₁ RRB ₁₁	0.3	1.3	1.3	-0.4	-1.8	-0.4	-2.1	-1.8	-0.7	-6.6	-13.4	2.7	2.0	1.3
6	B ₁₁ RRR ₁₁	0.1	1.3	1.3	-0.5	-2.0	-0.3	-2.5	-2.1	-0.7	-6.6	-14.6	2.6	1.9	0.0
7	fee B ₁₁ PLB ₁₁	-0.2	1.3	1.3	-0.3	-1.4	0.2	-2.8	-1.2	-1.6	-4.4	-12.0	3.2	2.2	3.4
8	ffe B ₁₁ PBR ₂₁	-0.1	1.3	1.3	-0.1	-1.4	0.1	-1.4	-1.0	-1.2	-3.2	-10.2	2.9	2.5	5.3
9	fff B ₁₁ PRB ₁₁	0.3	1.3	1.3	-0.4	-1.4	-0.2	-2.0	-1.2	-0.6	-6.8	-11.0	0.9	2.0	2.1
10	B ₁₁ LPB ₁₁	-0.1	1.3	1.3	-0.4	-1.6	0.3	-1.6	-0.4	-1.6	-7.0	-10.9	0.8	2.0	2.0
11	B ₁₁ LPR ₁₁	-0.1	1.3	1.3	-0.2	-1.6	0.1	-1.6	-0.4	-1.6	-7.4	-10.8	0.8	2.0	2.0
12	B ₁₁ PRR ₁₁	0.2	1.3	1.3	-0.3	-1.4	-0.3	-1.7	-1.2	-0.8	-7.3	-11.3	1.0	1.9	1.7

Table 4. Geometric parameters (degree) of the optimal conformations of Phe-Gly-Gly-Phe tetrapeptide molecule

Residues	Shape (conformation)			
	eff (B ₁₁ R R R ₁₁)	efe (B ₂₁ B L B ₁₁)	fff (B ₁₁ L P B ₁₁)	fee (B ₁₁ P L B ₁₁)
Phe 1	-67 161 176	-71 156 179	-80 166 179	-85 163 179
Gly2	-90 -69 180	-84 84 175	79 -74 176	79 -73 176
Gly3	-81 -62 -179	90 93 -179	-77 -51 -179	81 83 175
Phe 4	-150 -37 180	-147 151 180	-143 -43 180	-140 151 180
U_{rel} (kcal/mol)	0.0	1.8	1.7	3.4

Note: The values of dihedral angles are given in the sequence $\varphi, \psi, \omega, \chi^1, \chi^2, \dots$

The results can be used to study the spatial structure of tetrapeptide molecule as well as to study the conformational capabilities of side chains of the Phe1 and Phe4 when interacting with receptor molecules. The side chains of these residues have conformational freedom in the low-energy structures of the tetrapeptide molecule. Thus, the theoretical conformational analysis of this peptide molecule led to such structural organizations of molecules that do not exclude the realization by the molecule of a number of various functions that require strictly specific interactions with various receptors.

Figures 2 (a, b, c, d) represent schematically the backbone forms and positions of residues in low-energy conformations $B_{11}RRR_{11}$, $B_{21}BLB_{11}$, $B_{11}LPRB_{11}$ and $B_{11}PLB_{11}$ of the tetrapeptide molecule. The figures show that this molecule has folded N-terminal fragment of the molecule. Conformational possibilities of side chains of Phe1 and Phe4 in the best low energy conformations of peptide molecule have been investigated by plotting conformational maps. The conformational maps show that side chains of this residues have conformational freedom.

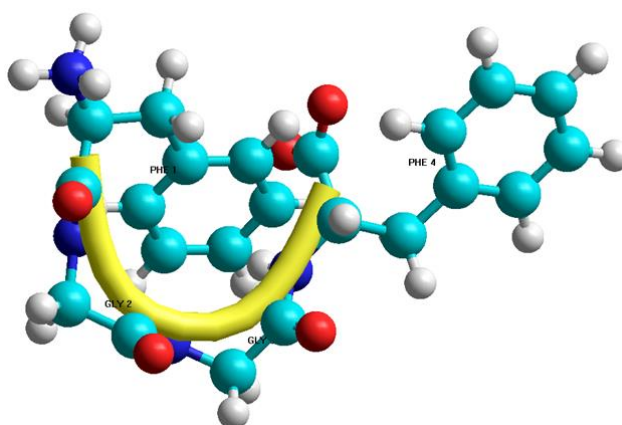
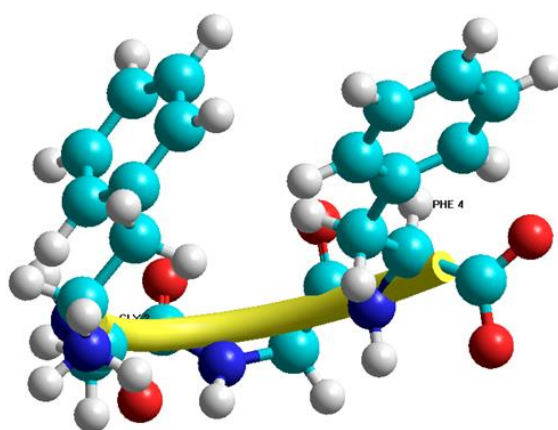


Figure 2a. Spatial structure of the low energy conformation $B_{11}RRR_{11}$ of the tetrapeptide molecule



Figures 2b. Spatial structure of the low energy conformation $B_{21}BLB_{11}$ of the tetrapeptide molecule

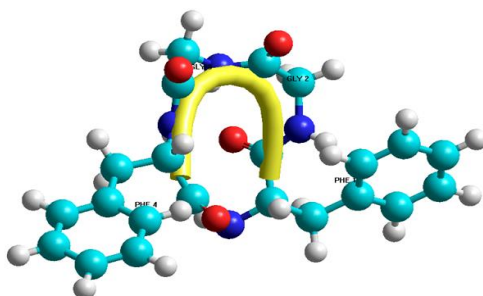


Figure 1c. Spatial structure of the low energy conformation B₁₁ L P B₁₁ of the tetrapeptide molecule

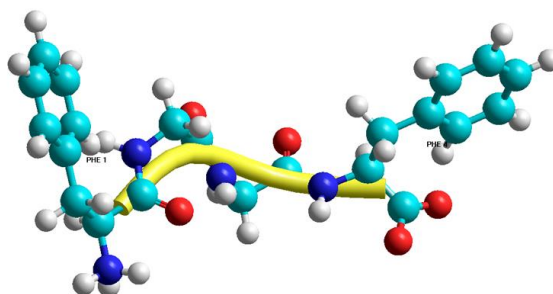


Figure 2d. Spatial structure of the low energy conformation B₁₁ P L B₁₁ of the tetrapeptide molecule

4. Conclusion

We have studied in detail the spatial structure and conformational properties of tri- and tetrapeptide molecules Phe1-Gly2-Gly3 and Phe1-Gly2-Gly3-Phe4. The conformational possibilities of these molecules were studied by the method of theoretical conformational analysis. The potential function of the system is chosen as the sum of non-valence, electrostatic and torsion interactions and the energy of hydrogen bonds. The low-energy conformations of these molecules, the values of the dihedral angles of the main and side chains of amino acid residues were found, the energy of intra- and inter-residual interactions was estimated. The spatial structure of the tripeptide and tetrapeptide molecules were calculated based on the low-energy conformations of the corresponding amino acid residues. It has been shown that the spatial structure of the tripeptide molecule can be represented by 15 low-energy conformations for four spatial structures and the spatial organization of the tetrapeptide can be represented by 12 low-energy conformations.

Conformational maps were constructed around the dihedral angles of the Phe1 and Phe4 side chains. The conformational maps show that almost complete conformational freedom is possible around the dihedral angles χ_1 of the Phe1 and Phe4 residues. The positions of the Phe1 and Phe4 side chains found by us are energetically the most favorable. It is revealed that low energy conformations of these molecules have the half-folded and folded type of backbone.

REFERENCES

1. Shamakina I.Yu., Shagiakhmetov F., Anokhin P.K., Kohan V.S., Davidiva T.V., (2021) The role of nociceptin in opioid regulation of brain functions. *Biomeditsinskaya Khimiya*, 67(1), pp. 5-16.
2. Witkin J.M., Statnick M.A., Rorick-Khin L.M., Pintar J.E. et al., (2014) The biology of Nociceptin/ Orphanin FQ(N/OFQ) related to obesity, stress, anxiety, mood, and drug dependence. *Pharmacol. Ther.*, 141(3), pp. 283-299.

3. Reha D., Valdes H., Vondrasek J., Hobza P. et al., (2005) Structure and IR spectrum of phenylalanyl-glycyl-glycine tripeptide in the gas-phase: IR/UV experiments ab initio quantum chemical calculations, and molecular dynamic simulations. *Chemistry, A European Journal*, 11 (23), pp. 6803-6817.
4. Ivanova E.A., Sarycheva N.Yu., Dubynin V.A., Malyshev A.V. et al., (2012) Behavioral effects of original tetrapeptide an analog of N-terminal nociceptin fragment. *Bulletin of Experimental Biology and Medicine*, 13(2), pp. 851-857.
5. Wilson K.R., Cruz M.J., Nicolas Ch., Belau L. et al. (2006) Thermal vaporization of biological nanoparticles: fragment-free vacuum ultraviolet photoionization mass spectra of tryptophan, phenylalanine- glycine-glycine, and beta-carotene. *J.Phys.Chem.*, 110(6) , pp .2106-2113.
6. Wtorek K., Janecka A. (2021) Potential of Nociceptin/Orphanin FQ Peptide Analogs for Drug Development. *Chem.Biodivers*, 18(1), p. 2000871.
7. Maksumov I. S., Ismailova L. I., Godjaev N. M., (1983) A computer program for calculation of conformations of molecular systems. *J. Struc. Chem.* , Vol. 24, pp. 147-148,
8. Ismailova L.I., Akverdieva G.A., Demukhamedova S.D., Akhmedov N.A., (2023) Molecular modelling of Pro-Gly gliproline and its complexes. *Moscow University Physics Bulletin*. 74(5), pp. 668-680.
9. Akhmedov N.A., Gadjiyeva Sh.N., Abbasli R.M., (2009) Structural organization of Asp-Pro-Lys-Gln-Asp-Phe-Met-Arg-Phe-NH₂ molecule. *Cur.Top. in Pept.&Prot.Res.*, Vol.10, pp. 57-62,.
10. Akhmedov N.A., Ismailova L.I., Agayeva L.N., Gocayev N.M., (2010) The spatial structure of the cardio active peptides, *Cur.Top. in Pept.&Prot. Res.*, Vol. 11, pp. 87-93.
11. Akhmedov N.A., Ismailova L.I., Abbasli R.M., Agayeva L.N., Akhmedova S.R., (2016) Spatial structure of Octarphin molecule, *IOSR JAP*, Vol. 8, pp. 66-70 ,
12. Akhmedov N., Agayeva L., Akverdieva G., Abbasli R., Ismailova L., (2021) Spatial structure of the ACTH-(6-9)-PGP molecule. *J.Chem.Soc.Pak.*, 43(5), pp. 500-504.
13. Akhmedov N., Agayeva L., Akhmedova S., Abbasli R., Ismailova L., (2021) Spatial structure of the β -Casomorphin-7 Molecule". *IOSR Journal of Applied Physics (IOSR-JAP)*, 13(5), pp.62-67.
14. Ismailova L.I., Abbasli R.M., Akhmedov N.A.,(2020) Computer modeling of the spatial astructure of nonapeptide molecule. Proceedings of the 7-th International Conference on Control and Optimization with Industrial Applications, Vol. I, pp. 218-220.
15. Ismailova L.I., Abbasli R.M., Akhedov N.A. (2022) Computer modeling of the spatial structure of hexapeptide molecule. Proceedings the 8-thInternational Conference on Control and Optimization with Industrial Applications, 24-26 August, Baku, Azerba law-erngyijan, (COIA 2022), Volume I, p. 249- 251.
16. Akhedov N.A., Agayeva L.N., Abbasli R.M., Ismailova L.I.,(2022) Computer modeling of law-energy spatial structures of casoxin G molecule. Proceedings the 8-thInternational Conference on Control and Optimization with Industrial Applications, 24-26 August, Baku, Azerba law-erngyijan, (COIA 2022), Vol. I, p. 63-65.
17. Исмаилова Л.И, Аббаслы Р.М., Ахмедов Н.А.,(2022) Трехмерная структура пента пептидной молекулы Arg-Glu-Arg-Gly-Pro. Научный журнал "Актуальные вопросы биологической физики и химии". Том 7, N 1, с.70-75, (In Russ).
18. Ismailova L.I. , Akhmedov N.A.,(2024) Spatial structure of the heptapeptide analog of Nociceptin molecule. *Mediterranean Journal of Chemistry* vol.14, N 2, pp. 105-111.
19. Ахмедов Н.А., Агаева L.N., Аббаслы R.M., Исмаилова L.I.(2024) Пространственная структура молекулы казоксина С. *Биофизика*, том 69, № 1, с. 1–9, (In Russ).
20. Popov E.M., (1985) An Approach to calculations of the problem of structure functional organization of natural reptides, *Mol. Biol.*, Vol. 19, pp. 1107-1138,
21. IUPAC-IUB,(1988) Quantity, Units and Symbols in Physical Chemistry, Vol. 39, Blackwell Scientific Publications, Oxford.

INSTRUCTIONS FOR AUTHORS

1. "The Baku Engineering University Journal-Physics" accepts original unpublished articles and reviews in the research field of the author.
2. Articles are accepted in English.
3. File format should be compatible with **Microsoft Word** and must be sent to the electronic mail (**journal@beu.edu.az**) of the Journal. The submitted article should follow the following format:
 - Article title, author's name and surname
 - The name of workplace
 - Mail address
 - Abstract and key words
4. The title of the article should be in each of the three languages of the abstract and should be centred on the page and in bold capitals before each summary.
5. **The abstract** should be written in **9 point** type size, between **100** and **150** words. The abstract should be written in the language of the text and in two more languages given above. The abstracts of the article written in each of the three languages should correspond to one another. The keywords should be written in two more languages besides the language of the article and should be at least three words.
6. **UDC** and **PACS** index should be used in the article.
7. The article must consist of the followings:
 - Introduction
 - Research method and research
 - Discussion of research method and its results
 - In case the reference is in Russian it must be given in the Latin alphabet with the original language shown in brackets.
8. **Figures, pictures, graphics and tables** must be of publishing quality and inside the text. Figures, pictures and graphics should be captioned underneath, tables should be captioned above.
9. **References** should be given in square brackets in the text and listed according to the order inside the text at the end of the article. In order to cite the same reference twice or more, the appropriate pages should be given while keeping the numerical order. For example: [7, p.15].

Information about each of the given references should be full, clear and accurate. The bibliographic description of the reference should be cited according to its type (monograph, textbook, scientific research paper and etc.) While citing to scientific research articles, materials of symposiums, conferences and other popular scientific events, the name of the article, lecture or paper should be given.

Samples:

- a) **Article:** Demukhamedova S.D., Aliyeva İ.N., Godjajev N.M.. *Spatial and electronic structure of monomerrik and dimeric conapeetes of carnosine üith zinc*, Journal of structural Chemistry, Vol.51, No.5, p.824-832, 2010
 - b) **Book:** Christie ohn Geankoplis. *Transport Processes and Separation Process Principles*. Fourth Edition, Prentice Hall, p.386-398, 2002
 - c) **Conference paper:** Sadychov F.S., Aydın C., Ahmedov A.İ.. Appligation of Information – Commu-nication Technologies in Science and education. II International Conference."Higher Twist Effects In Photon- Proton Collisions", Baki, 01-03 Noyabr, 2007, ss 384-391
References should be in 9-point type size.
10. The margins sizes of the page: - Top 2.8 cm. bottom 2.8 cm. left 2.5 cm, right 2.5 cm. The article main text should be written in Palatino Linotype 11 point type size single-spaced. Paragraph spacing should be 6 point.
 11. The maximum number of pages for an article should not exceed 15 pages
 12. The decision to publish a given article is made through the following procedures:
 - The article is sent to at least to experts.
 - The article is sent back to the author to make amendments upon the recommendations of referees.
 - After author makes amendments upon the recommendations of referees the article can be sent for the publication by the Editorial Board of the journal.